JOURNAL OF GEOPHYSICAL RESEARCH, VOL. 114, B04412, doi:10.1029/2008JB006166, 2009

Click Here for Full Article

Fault friction parameters inferred from the early stages of afterslip following the 2003 Tokachi-oki earthquake

Jun'ichi Fukuda,[1] Kaj M. Johnson,[1] Kristine M. Larson,[2] and Shin'ichi Miyazaki[3]

Received 16 October 2008; revised 9 January 2009; accepted 3 February 2009; published 25 April 2009.

[1] We use subdaily GPS time series of positions in the first 5 hours following the 2003 Tokachi-oki earthquake (M_w = 8.0) located offshore of Hokkaido, Japan, to estimate frictional parameters for the afterslip zone on the subduction interface. The data show little motion immediately after the earthquake with sudden acceleration at about 1.2 hours after the main shock. This coincides with the largest aftershock (M = 7.4), followed by gradual deceleration. We assume that early afterslip is the response of a fault patch to instantaneous stress perturbations caused by the main shock and the largest aftershock. Early afterslip is modeled with a spring-slider system obeying a rate- and state-dependent friction law. We develop and apply an inversion method to estimate friction parameters, D_c, $a\sigma$, and $(a - b)\sigma$, where σ is effective normal stress. The estimated 95% confidence intervals of D_c, $a\sigma$, and $(a - b)\sigma$ are 2.6×10^{-4} to 1.8×10^{-3} m, 0.29 to 0.43 MPa, and 0.214 to 0.220 MPa, respectively. Estimated D_c is 10 to 10^3 times larger than typical laboratory values. Estimated $a\sigma$ and $(a - b)\sigma$ values suggest that a and $a - b$ are smaller than typical laboratory values and/or the pore pressure on the plate boundary is significantly elevated above the hydrostatic value. Our analyses show that the model can reproduce the observed GPS data and that the timing of the rapid acceleration of postseismic deformation is controlled by the frictional properties of the fault and stress change from the main shock, not by the timing of the largest aftershock.

Citation: Fukuda, J., K. M. Johnson, K. M. Larson, and S. Miyazaki (2009), Fault friction parameters inferred from the early stages of afterslip following the 2003 Tokachi-oki earthquake, *J. Geophys. Res.*, *114*, B04412, doi:10.1029/2008JB006166.

1. Introduction

[2] The 2003 Tokachi-oki earthquake (M_w = 8.0) ruptured the plate boundary along the Kuril trench, offshore Hokkaido island, northeastern Japan, where the Pacific plate subducts beneath Hokkaido (Figure 1). The plate interface is strongly coupled with a slip deficit rate of about 80 mm/a [*Suwa et al.*, 2006]. The main shock occurred at 19:50 (UTC) on 25 September 2003 and was followed by the largest aftershock (M = 7.4) at 21:08 on the same day. The rupture area of the main shock is close to that of the 1952 Tokachi-oki earthquake (M = 8.1) [*Yamanaka and Kikuchi*, 2003]. Following the main shock, postseismic deformation was recorded by a continuous GPS network, GEONET. This postseismic deformation has been interpreted as a result of afterslip on the plate interface [*Miura et al.*, 2004; *Miyazaki et al.*, 2004; *Ozawa et al.*, 2004; *Baba et al.*, 2006]. *Miyazaki et al.* [2004] and *Ozawa et al.* [2004] estimated the space-time evolution of afterslip using daily GPS station positions and found that decaying afterslip distributed around the rupture region can fit the data well. *Miyazaki and Larson* [2008] estimated GPS station positions every 30 seconds for the first 4 hours following the main shock and inverted the station positions to infer space-time evolution of afterslip. Their results show that postseismic deformation immediately after the main shock can be explained by afterslip.

[3] Recently, *Larson and Miyazaki* [2008] estimated subdaily GPS station positions after the 2003 Tokachi-oki earthquake using an improved GPS analysis technique that separated postseismic deformation in the first 24 hours following the main shock from displacements caused by the main shock and the largest aftershock. Figure 2 shows the GPS station positions every 12 minutes for the first 5 hours following the main shock. The data show little motion immediately after the main shock with sudden acceleration at about 1.2 hours following the main shock at the time of the largest aftershock, suggesting acceleration of afterslip at this time.

[4] Most previous frictional afterslip studies have modeled afterslip using a rate- and state-dependent friction law or a simplified rate-dependent, velocity-strengthening version of the friction law [*Marone et al.*, 1991; *Linker and Rice*, 1997; *Hearn et al.*, 2002; *Montési*, 2004; *Perfettini and Avouac*, 2004, 2007; *Perfettini et al.*, 2005]. The

[1]Department of Geological Sciences, Indiana University, Bloomington, Indiana, USA.
[2]Department of Aerospace Engineering Sciences, University of Colorado, Boulder, Colorado, USA.
[3]Department of Geophysics, Graduate School of Science, Kyoto University, Kyoto, Japan.

Copyright 2009 by the American Geophysical Union.
0148-0227/09/2008JB006166$09.00

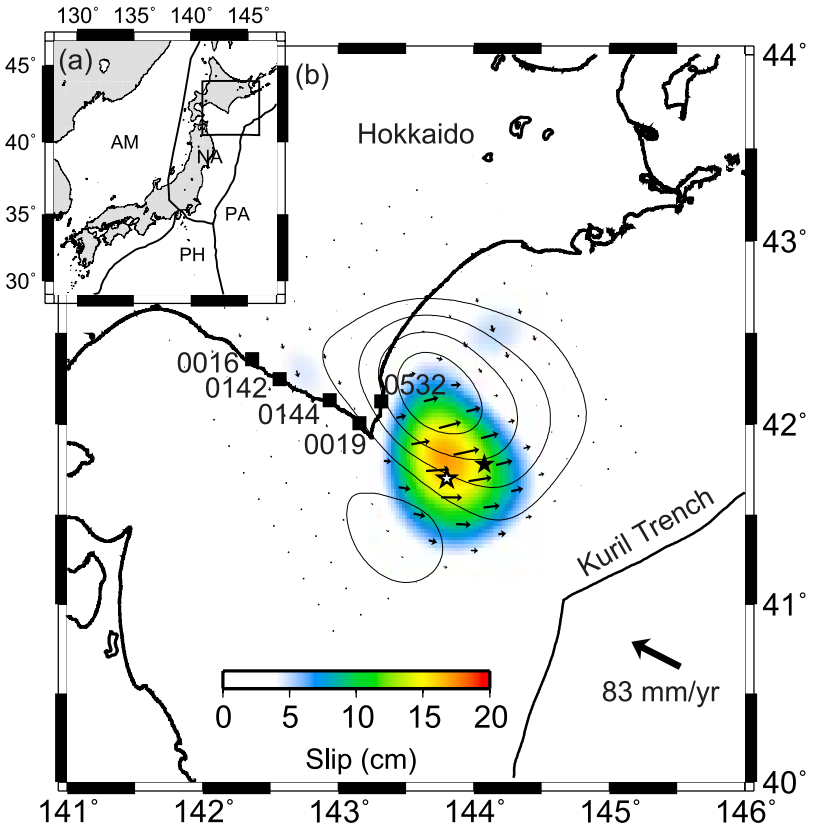

Figure 1. (a) Tectonic setting of the Japanese islands. Solid lines indicate plate boundaries. AM, PH, PA, and NA denote Amurian, Philippine Sea, Pacific and North American plates, respectively. (b) Magnified map of rectangular area in Figure 1a. Solid squares show GPS stations used in this study. Solid and open stars denote epicenters of the 2003 Tokachi-oki earthquake and its largest aftershock, respectively. Color scale and vectors show cumulative afterslip for 5 hours following the main shock. Contours with 1-m interval represent coseismic slip distribution of the main shock estimated by *Miyazaki and Larson* [2008]. Thick arrow shows the relative motion of the Pacific plate with respect to the North American plate computed based on the work of *DeMets et al.* [1994].

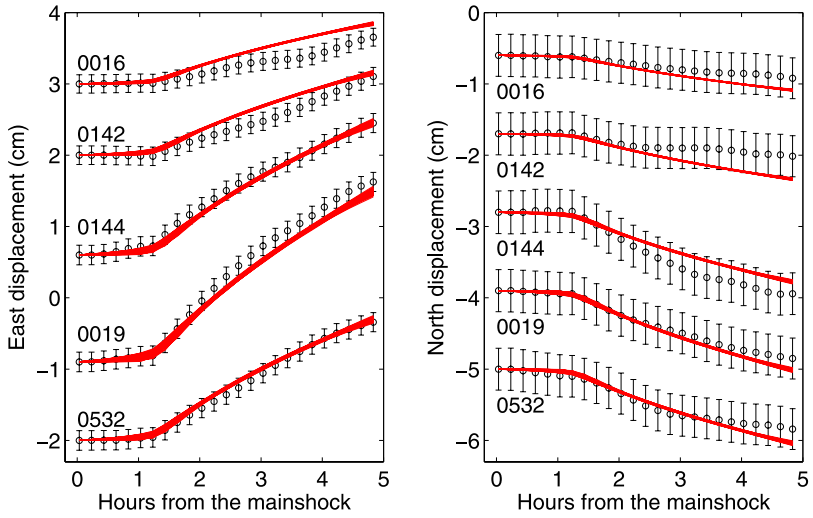

Figure 2. GPS time series at the five stations shown in Figure 1. See Figure 1 for station locations. Left and right plots show east and north components, respectively. GPS solutions are shown with open circles. Error bars denote 2σ uncertainties for east component and 1σ uncertainties for north component. Each solid curve denotes predicted surface displacements from a Monte Carlo sample of the posterior PDF shown in Figure 7.

"slowness law" version of rate- and state-dependent friction law [*Dieterich*, 1979, 1981; *Ruina*, 1983] is

$$\tau = \sigma\left[\mu* + a\ln\left(\frac{V}{V*}\right) + b\ln\left(\frac{V*\theta}{D_c}\right)\right] \quad (1)$$

$$\frac{\mathrm{d}\theta}{\mathrm{d}t} = 1 - \frac{V\theta}{D_c}, \quad (2)$$

where τ is shear stress, V is slip velocity, θ is a state variable, a and b are dimensionless constants, D_c is a characteristic slip distance for the evolution of θ, σ is effective normal stress that is assumed to be independent of time, $V*$ is a reference velocity, and $\mu*$ is the friction coefficient at steady state velocity $V*$.

[5] If θ does not vary with time (i.e., $d\theta/dt = 0$), equations (1) and (2) reduces to the simpler steady state expression

$$\tau_{ss} = \sigma\left[\mu* + (a-b)\ln\left(\frac{V}{V*}\right)\right], \quad (3)$$

where τ_{ss} is the steady state frictional stress. $a - b$ represents the velocity dependence of the steady state frictional stress. For $a - b > 0$, τ_{ss} evolves to a higher value when the velocity increases and for $a - b < 0$, τ_{ss} evolves to a lower value. These conditions are referred to as velocity strengthening friction and velocity weakening friction, respectively. Velocity strengthening portions of a fault are nominally stable, that is, they do not spontaneously rupture. Velocity weakening portions of a fault can undergo spontaneous rupture under appropriate conditions [e.g., *Ruina*, 1983; *Gu et al.*, 1984; *Ranjith and Rice*, 1999]. The velocity-strengthening friction law given by equation (3) with $a - b > 0$, which is effectively a nonlinear viscous rheology, predicts logarithmic time evolution of afterslip, or, equivalently, $1/t$ decay of slip velocity in response to a sudden coseismic stress increase [*Marone et al.*, 1991; *Perfettini and Avouac*, 2004]. Models incorporating this law are able to fit decaying postseismic deformation measurements [*Marone et al.*, 1991; *Linker and Rice*, 1997; *Hearn et al.*, 2002; *Montési*, 2004; *Perfettini and Avouac*, 2004, 2007; *Perfettini et al.*, 2005].

[6] Numerical simulations using the full rate- and state-dependent friction law generate afterslip on velocity-strengthening regions of faults [e.g., *Tse and Rice*, 1986; *Marone et al.*, 1991]. *Johnson et al.* [2006] showed that a numerical model incorporating this law can fit postseismic deformation measurements after the 2004 Parkfield earthquake. In contrast to the velocity-strengthening friction law, the full rate- and state-dependent friction law generates an acceleration phase of afterslip after a sudden stress increase for sufficiently compliant systems [*Rice and Gu*, 1983; *Perfettini and Ampuero*, 2008] and predicts time evolution of slip similar to that predicted by the velocity strengthening friction law after the acceleration phase [*Perfettini and Ampuero*, 2008]. *Perfettini and Ampuero* [2008] showed that the duration of the acceleration phase is dependent on frictional properties on the fault. This suggests that the acceleration of afterslip following the 2003 Tokachi-oki earthquake may be explained by a model incorporating the rate- and state-dependent friction law and that the observations recording the acceleration of afterslip may provide constraints on frictional properties on the subduction interface.

[7] The rate- and state-dependent friction law has been used in numerical simulations of generic earthquake cycles to model slip behavior including seismic slip, earthquake nucleation, afterslip, and transient aseismic slip [*Tse and Rice*, 1986; *Rice*, 1993; *Kato*, 2004; *Liu and Rice*, 2005]. Numerical simulations with the friction law have also been applied with observational constraints for specific faults such as the Parkfield segment of the San Andreas fault [*Stuart and Tullis*, 1995], the Suruga and the Nankai troughs, southwestern Japan [*Stuart*, 1988; *Kato and Hirasawa*, 1999; *Hori et al.*, 2004], and the Sanriku region along the Japan trench [*Kato*, 2008] to understand complex seismic and aseismic slip histories and preseismic slip. These numerical simulations require specification of values of the friction parameters D_c, a, and b which control frictional properties on faults and thus determine temporal and spatial slip behavior.

[8] Friction parameters D_c, a, b, and $a - b$ have been inferred from laboratory measurements [e.g., *Blanpied et al.*, 1995, 1998; *Paterson and Wong*, 2005]. Postseismic geodetic data have also been used to infer $(a - b)\sigma$ [*Hearn et al.*, 2002; *Perfettini and Avouac*, 2004, 2007; *Miyazaki et al.*, 2004; *Perfettini et al.*, 2005; *Hsu et al.*, 2006] and D_c, $a\sigma$, and $b\sigma$ [*Johnson et al.*, 2006]. Laboratory measurements show a strong dependence of $a - b$ on temperature, and consequently, depth. *Blanpied et al.* [1995] used experiments on wet granite gouge to infer $a - b$ of order 10^{-3} for temperatures below 400°C and of order 10^{-2} and increasing roughly linearly with temperature above 400°C. Many numerical simulations adopt a depth distribution of $a - b$ consistent with the laboratory results [e.g., *Kato and Hirasawa*, 1999; *Lapusta and Rice*, 2003; *Liu and Rice*, 2005]. Studies utilizing postseismic geodetic data and the velocity strengthening friction law consistently report $(a - b)\sigma$ values in the range 0.2–0.7 MPa [*Hearn et al.*, 2002; *Perfettini and Avouac*, 2004, 2007; *Miyazaki et al.*, 2004; *Perfettini et al.*, 2005; *Hsu et al.*, 2006], which corresponds to $a - b$ of order 10^{-4}–10^{-3} on faults with hydrostatic pore pressure at subseismogenic depths. This is about an order of magnitude smaller than laboratory values, suggesting $a - b$ for real faults is actually smaller than for laboratory samples, and/or elevated pore pressure in real faults. Laboratory measurements of the characteristic slip distance, D_c, are generally in the range 10^{-6}–10^{-4} m [*Marone*, 1998; *Paterson and Wong*, 2005]; however numerical limitations preclude the use of such small D_c in simulations. Numerical simulations typically adopt D_c values of order 10^{-3} to 10^{-1} m.

[9] There has been much discussion regarding the range of characteristic slip distance, D_c, for real faults. It is argued that laboratory measurements of the characteristic slip distance must be scaled appropriately to obtain values for real faults [*Marone*, 1998]. It has been proposed that the characteristic slip distance for real faults is several orders of magnitude larger than the laboratory-measured range based on considerations on contact topography of fault surface [*Scholz*, 1988] or gouge zone thickness [*Marone and*

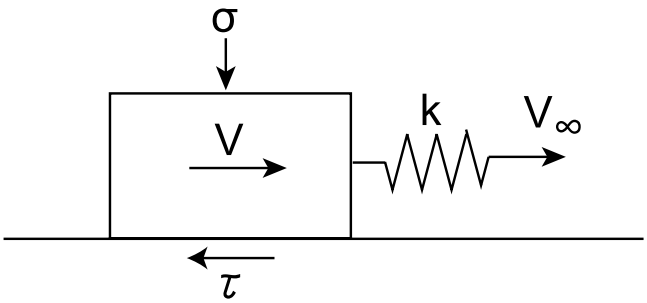

Figure 3. Spring-slider model used to model afterslip on a fault patch. A rigid slider with unit base area is connected to an elastic spring of stiffness k. The spring is dragged at constant velocity V_∞. V is velocity of the slider, τ is frictional stress applied on the base of the slider, and σ is effective normal stress.

Kilgore, 1993]. In contrast, *Lapusta and Rice* [2003] argued that the characteristic slip distance for real faults is in the laboratory-measured range based on the sizes of the smallest earthquakes. Constraining possible ranges of the friction parameters based on geophysical observations is important for simulation studies, especially for simulations applied to observations associated with slip on real faults.

[10] In this study, we model early postseismic deformation of the 2003 Tokachi-oki earthquake assuming that the observed GPS signal is a response to afterslip on the plate interface in order to address the following questions: (1) Why was there a 1.2 hour delay in rapid acceleration of afterslip following the main shock? (2) Did the main shock or the largest aftershock trigger the afterslip? (3) What friction parameters are consistent with the observations? To address these questions, we model afterslip using a single degree of freedom spring-slider model [e.g., *Rice and Gu*, 1983] that is assumed to obey a rate- and state-dependent friction law. A nonlinear inversion scheme is developed and applied to estimate rate-state friction parameters. We show that the subdaily GPS data can be explained by the spring-slider model and that the inversion places tight constraints on the friction parameters. Furthermore, we show that the timing of the rapid acceleration of afterslip is largely controlled by the frictional properties of the fault and stress change from the main shock, not by the timing of the largest aftershock.

2. GPS Data and Forward Model

2.1. GPS Data

[11] We use the GPS station positions estimated by *Larson and Miyazaki* [2008] every 12 minutes for the first 5 hours following the main shock. Position time series from the five stations shown in Figure 1, which contain large postseismic signals, are used in this study and shown in Figure 2. Coseismic offsets from the largest aftershock, estimated by *Larson and Miyazaki* [2008], have been removed from the time series. Only horizontal components are used. Vertical components are excluded because of their low signal-to-noise ratio. These time series show little motion immediately after the main shock and sudden acceleration at about 1.2 hours following the main shock. The time of the sudden acceleration coincides with the time of the largest aftershock.

2.2. Forward Model

2.2.1. Governing Equations

[12] We assume that afterslip is a response of a fault patch adjacent to the coseismic rupture to instantaneous stress perturbations caused by the main shock and the largest aftershock. We model slip on the fault patch using the single degree of freedom spring-slider model [e.g., *Rice and Gu*, 1983] shown in Figure 3. The fault patch in an elastic medium is modeled as a rigid block with unit base area connected to a spring of stiffness k. The spring is loaded at constant velocity V_∞ which represents the steady state creep rate just before the main shock in the region of afterslip. The frictional shear stress applied on the base of the slider, τ, can be related to slip of the slider, assuming quasi-static slip, as

$$\frac{\mathrm{d}\tau}{\mathrm{d}t} = k(V_\infty - V), \tag{4}$$

where V is slip velocity of the slider. The shear stress τ is assumed to obey the "slowness law" version of the rate- and state-dependent friction law given by equations (1) and (2). Equations (4), (1), and (2) along with initial conditions fully describe the motion of the slider.

[13] Differentiating equation (1) with respect to time and then combining it with equation (4), we have

$$\frac{\mathrm{d}V}{\mathrm{d}t} = \frac{V}{a\sigma}\left[k(V_\infty - V) - \frac{b\sigma}{\theta}\frac{\mathrm{d}\theta}{\mathrm{d}t}\right]. \tag{5}$$

The system of differential equations for V and θ, which consists of equations (2) and (5), can be solved numerically to yield the solution, $V(t)$ and $\theta(t)$, if the parameters D_c, $a\sigma$, $b\sigma$, k, and V_∞, and initial conditions for V and θ are specified.

2.2.2. Initial Conditions

[14] We express the effect of the main shock on the afterslip patch by applying an instantaneous shear stress step $\Delta\tau$ to the slider at $t = 0$. Let V_0^- and θ_0^- be values of V and θ before the main shock, and let V_0^+ and θ_0^+ be those immediately after the main shock. We assume that the spring-slider system is in steady state ($d\theta/dt = 0$) before the main shock. *Johnson et al.* [2006] showed that this is a reasonable assumption for a spring-slider system with $a - b > 0$ as long as $a - b$ is of the same order of magnitude as a and D_c is on the order of 0.01 m or less. These conditions are satisfied in the present study as shown in section 4. Under the steady state assumption before the main shock, θ_0^- is given by $\theta_0^- = D_c/V_0^-$. Because the main shock is modeled as an instantaneous event, θ does not evolve during the main shock, i.e., $\theta_0^+ = \theta_0^- = D_c/V_0^-$. From equation (1) and $\theta_0^+ = \theta_0^-$, the slip velocity immediately after the main shock is given by $V_0^+ = V_0^- \exp(\Delta\tau/a\sigma)$. Therefore specification of V_0^-, $\Delta\tau$, D_c, and $a\sigma$ determines V_0^+ and θ_0^+, values of V and θ immediately after the main shock. Velocity and state between the main shock and the largest aftershock, $V(t)$ and

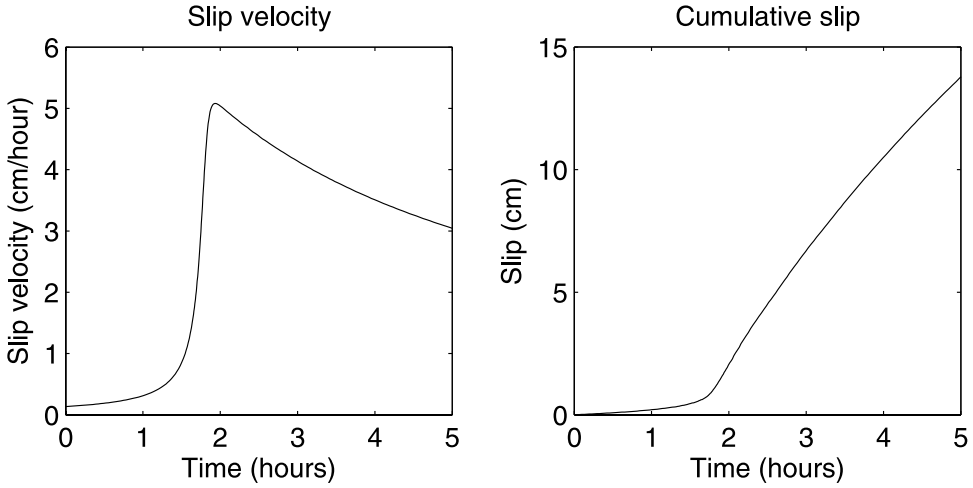

Figure 4. Time evolution of slip velocity and cumulative slip of the slider in response to a shear stress step at $t = 0$. The parameters in the spring-slider model are set to $D_c = 1.0 \times 10^{-3}$ m, $a\sigma = 0.40$ MPa, $b\sigma = 0.17$ MPa, $k = 1.0$ MPa/m, $V_\infty = V_0^- = 0.08$ m/a, $\Delta\tau = 2.0$ MPa, and $\Delta\tau_{\mathrm{aft}} = 0.0$ MPa.

$\theta(t)$, are obtained by solving equations (2) and (5) with initial conditions

$$\theta(0) = \theta_0^+ = \frac{D_c}{V_0^-} \tag{6}$$

and

$$V(0) = V_0^+ = V_0^- \exp\left(\frac{\Delta\tau}{a\sigma}\right). \tag{7}$$

[15] The effect of the largest aftershock on the afterslip patch is also taken into consideration by imposing an instantaneous shear stress step $\Delta\tau_{\mathrm{aft}}$ to the slider at the time of the largest aftershock, $t = t_{aft}$. Let $V^-(t_{aft})$ and $\theta^-(t_{aft})$ be values of V and θ immediately before the largest aftershock, and let $V^+(t_{aft})$ and $\theta^+(t_{aft})$ be those immediately after the aftershock. $V^-(t_{aft})$ and $\theta^-(t_{aft})$ are determined by solving equations (2) and (5) as described above. Similarly to the case of the main shock, $\theta^+(t_{aft})$ and $V^+(t_{aft})$ are given by $\theta^+(t_{aft}) = \theta^-(t_{aft})$ and $V^+(t_{aft}) = V^-(t_{aft}) \exp(\Delta\tau_{\mathrm{aft}}/a\sigma)$, respectively. Velocity and state after the largest aftershock, $V(t)$ and $\theta(t)$ ($t > t_{aft}$), are obtained by solving equations (2) and (5) with initial conditions

$$\theta(t_{aft}) = \theta^+(t_{aft}) = \theta^-(t_{aft}) \tag{8}$$

and

$$V(t_{aft}) = V^+(t_{aft}) = V^-(t_{aft}) \exp\left(\frac{\Delta\tau_{aft}}{a\sigma}\right). \tag{9}$$

2.2.3. Simulations

[16] In this section, we show that the forward model described in sections 2.2.1 and 2.2.2 predicts an acceleration phase of afterslip. We then show some numerical simulations to illustrate the influence of the friction parameters on afterslip history.

[17] Figure 4 shows the time evolution of slip velocity and cumulative slip of the slider obtained from equations (2) and (5) with initial conditions described above. The parameters in the spring-slider model are set to $D_c = 1.0 \times 10^{-3}$ m, $a\sigma = 0.40$ MPa, $b\sigma = 0.17$ MPa, $k = 1.0$ MPa/m, $V_\infty = V_0^- = 0.08$ m/a, and $\Delta\tau = 2.0$ MPa. We neglect the effect of the largest aftershock in Figure 4, i.e. $\Delta\tau_{\mathrm{aft}} = 0.0$ MPa. Figure 4 shows that slip accelerates very slowly immediately after the main shock, and then accelerates rapidly at about 1.6 hours after the main shock. The time evolution of slip is qualitatively consistent with the observed evolution of postseismic deformation shown in Figure 2. This simulation indicates that an imposed instantaneous stress change at $t = 0$ can produce delayed acceleration of slip without imposing stress changes at $t > 0$.

[18] *Perfettini and Ampuero* [2008] showed that a single degree of freedom spring-slider model and a two-dimensional fault governed by the rate- and state-dependent friction with velocity strengthening frictional properties ($a - b > 0$) under initial conditions similar to equations (6) and (7) generate an acceleration phase of afterslip which is analogous to that shown in Figure 4 under appropriate conditions. *Perfettini and Ampuero* [2008] found that the state θ is well above the steady state value immediately after an imposed stress step and gradually evolves to the steady state value which is approximately reached when the velocity attains its maximum value. They obtained approximate analytical expressions for the maximum velocity, $V_{\max}$, and the time when the maximum velocity is reached, $t_{\max}$, for a spring-slider model with spring stiffness sufficiently smaller than $b\sigma/D_c$

$$V_{\max} \approx V_0^- \exp\left[\frac{\Delta\tau}{(a-b)\sigma}\right] \tag{10}$$

$$t_{\max} \approx \frac{a}{b}\frac{D_c}{V_0^-} \exp\left(-\frac{\Delta\tau}{a\sigma}\right). \tag{11}$$

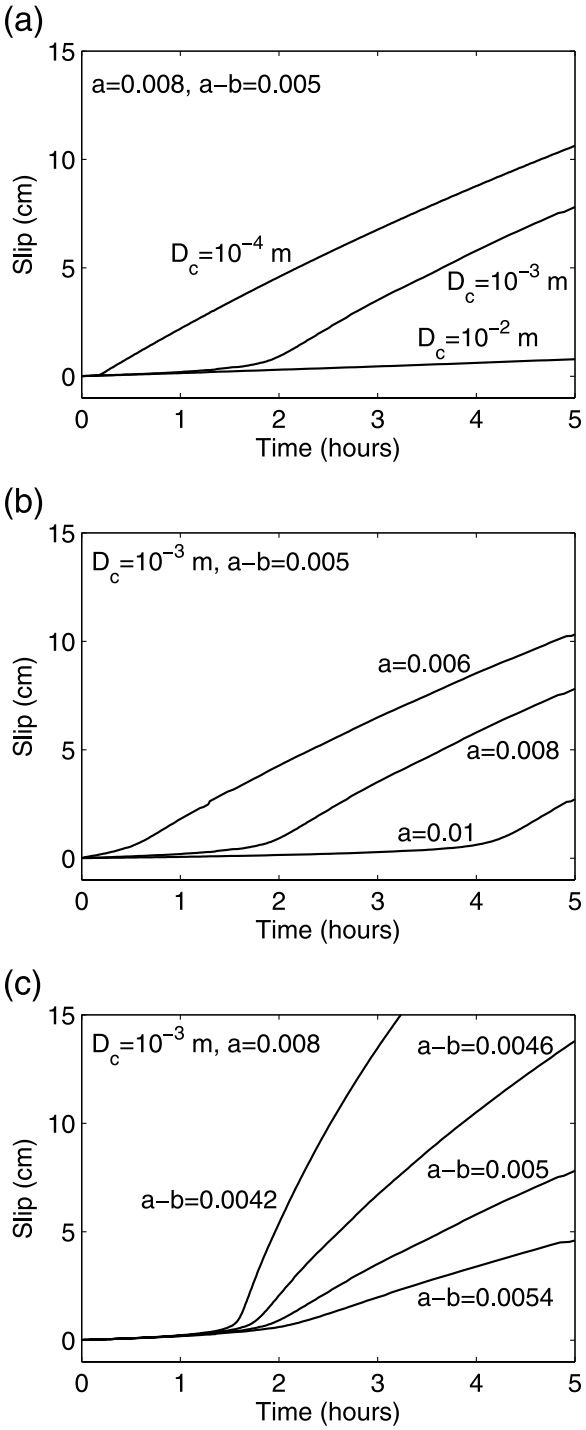

Figure 5. Cumulative slip of the slider with time for different values of D_c, a, and $a - b$. (a) Slip histories for different values of D_c with a and $a - b$ fixed. (b) Slip histories for different values of a with D_c and $a - b$ fixed. (c) Slip histories for different values of $a - b$ with D_c and a fixed. Parameters other than D_c, a, and $a - b$ are fixed to the following values: σ = 50 MPa, k = 1.0 MPa/m, $V_\infty = V_0^- = 0.08$ m/a, $\Delta\tau$ = 2.0 MPa, $\Delta\tau_{aft}$ = 0.0 MPa.

Perfettini and Ampuero [2008] showed that equations (10) and (11) are reasonable approximations for a two-dimensional fault model if the spatial extent of the size of coseismic stress perturbation is sufficiently larger than $GD_c/b\sigma$ where G is the shear modulus. After the time of the maximum velocity, decelerating slip evolution is similar to that predicted by steady state velocity strengthening friction (equation (3)) [*Perfettini and Ampuero*, 2008]. Their study suggests that the acceleration phase of afterslip ($0 < t < t_{max}$) may be useful to constrain D_c, a, b, and $a - b$ because V_{max} and t_{max} are dependent on these parameters (equations (10) and (11)). On the other hand, the deceleration phase of afterslip ($t > t_{max}$) may be useful to constrain $a - b$ because the deceleration phase is suggested to be well described by the steady state velocity strengthening friction which depends on $a - b$ but not on D_c, a, and b.

[19] Figure 5 shows slip histories of the slider for different values of D_c, a, and $a - b$ with the other parameters fixed to σ = 50 MPa, k = 1.0 MPa/m, $V_\infty = V_0^- = 0.08$ m/a, $\Delta\tau$ = 2.0 MPa, and $\Delta\tau_{aft}$ = 0.0 MPa, for 5 hours following the shear stress step at t = 0. Figure 5 shows that the time evolution of slip is sensitive to values of D_c, a, and $a - b$. Figure 5a shows slip histories for different values of D_c with a and $a - b$ fixed. We can see that time to rapid acceleration strongly depends on D_c; a larger D_c value generates a more delayed rapid acceleration. This is consistent with t_{max} given by equation (11). Figure 5b, which shows slip histories for different values of a with D_c and $a - b$ fixed, indicates that time to rapid acceleration also depends on a; a larger a value generates a more delayed rapid acceleration, which is also consistent with t_{max} given by equation (11). Figure 5c shows slip histories for different values of $a - b$ with D_c and a fixed. Although time to rapid acceleration is not very sensitive to $a - b$, maximum slip velocity has strong dependence on $a - b$; a smaller $a - b$ value results in a larger maximum slip velocity, which is consistent with V_{max} given by equation (10). In addition, slip magnitude for the period shown in Figure 5c also strongly depends on $a - b$. These high sensitivities of slip evolution to friction parameters suggest that we can estimate the friction parameters from postseismic deformation immediately after the earthquake.

[20] Figure 6 shows slip histories computed with the same parameter values as those in Figure 5 for 7 days after the stress step. Figures 6a and 6b show that the spring-slider model predicts similar slip histories for different D_c and a values except during the very early period, suggesting that it is difficult to constrain D_c and a from daily GPS data. On the other hand, slip histories for different $a - b$ values (Figure 6c) show that the magnitude of afterslip is highly dependent on $a - b$ values, suggesting that $a - b$ can be estimated from daily GPS data. The strong dependence of the longer timescale slip histories on $a - b$ and the weak dependence on D_c and a are compatible with the fact that the deceleration phase is well described by the steady state velocity strengthening friction [*Perfettini and Ampuero*, 2008]. Comparison of Figures 5 and 6 indicates that the slip evolution for the first few hours to 1 day following the stress step is much more sensitive to D_c and a than the slip evolution over longer periods. Therefore the subdaily GPS data following the 2003 Tokachi-oki earthquake provides a unique opportunity to infer D_c and a from data.

2.2.4. Calculation of Model-Predicted Surface Displacements

[21] In section 3, we develop an inversion method for estimating the parameters in the spring-slider model from the subdaily GPS time series. To invert the GPS time series,

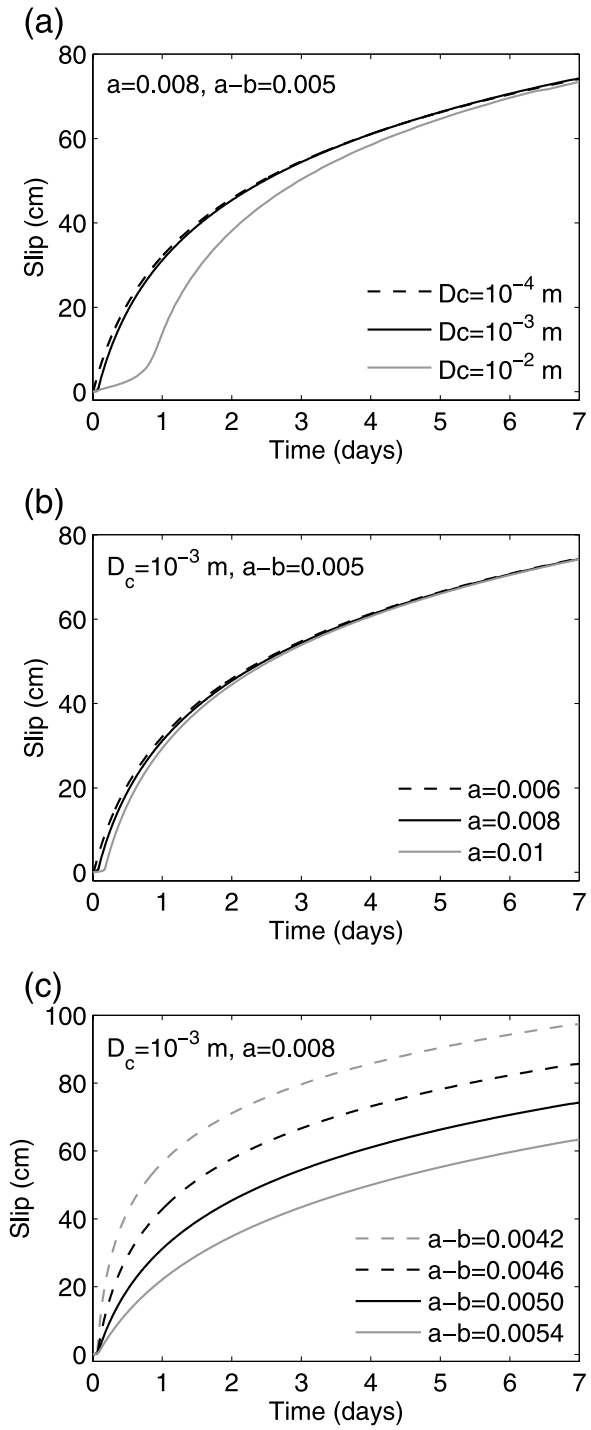

Figure 6. Cumulative slip of the slider with time for different values of D_c, a, and $a - b$. (a) Slip histories for different values of D_c with a and $a - b$ fixed. (b) Slip histories for different values of a with D_c and $a - b$ fixed. (c) Slip histories for different values of $a - b$ with D_c and a fixed. Other parameters (σ, k, V_∞, V_0^-, $\Delta\tau$, and $\Delta\tau_{aft}$) are fixed to the same values as those in Figure 5.

it is necessary to relate time evolution of the slip velocity of the slider, $V(t)$, to surface displacements at the GPS stations. For this purpose, we invert cumulative 5-hour postseismic displacements at 35 GPS stations for distributed afterslip on the plate interface assuming a homogeneous elastic half-space [*Okada*, 1985]. We approximate the geometry of the plate interface by a planar fault summarized in Table 1 following the plate interface configuration given by *Katsumata et al.* [2003] and *Earthquake Research Committee* [2003]. We obtain cumulative afterslip distribution on the fault plane for the first 5 hours following the main shock by minimizing the sum of squared norms of misfit and slip roughness

$$\Phi(\mathbf{s}) = \|\boldsymbol{\Sigma}_y^{-1/2}(\mathbf{y} - \mathbf{G}\mathbf{s})\|^2 + \beta^2 \|\mathbf{D}\mathbf{s}\|^2, \tag{12}$$

where $\mathbf{y}$ is a vector of cumulative postseismic displacements, $\boldsymbol{\Sigma}_y$ is the covariance matrix of measurement errors, $\mathbf{s}$ is a vector of slip, $\mathbf{G}$ is a matrix of Green's functions [*Okada*, 1985], $\mathbf{D}$ is a matrix of the finite difference approximation of the Laplacian operator, and β^2 is a parameter which determines the weight of the smoothness constraints. In the inversion, the slip direction is constrained within ±45° of the reverse direction of the motion of the subducting Pacific plate. The weighting parameter β^2 is selected subjectively to give a qualitatively smooth slip distribution. The estimated afterslip for 5 hours following the earthquake is shown in Figure 1.

[22] We assume that the afterslip distribution at any time is proportional to this slip distribution and the temporal variation of slip is assumed to be governed by slip of the slider. Under these assumptions, model-predicted displacements at the GPS stations at time t, $\hat{\mathbf{d}}(t)$, are given by

$$\hat{\mathbf{d}}(t) = [\mathbf{G}\bar{\mathbf{s}}]f(t), \tag{13}$$

where $\mathbf{G}$ is the matrix of Green's functions for the kinematic slip inversion, $\bar{\mathbf{s}}$ is the vector of the slip distribution obtained from the kinematic inversion (Figure 1) normalized by the maximum value of $\mathbf{s}$, and $f(t) = \int_0^t V(t')dt'$ is a scalar function of time which represents cumulative slip of the slider. Note that in equation (13), $\mathbf{G}$ and $\bar{\mathbf{s}}$ are known, whereas $f(t)$ depends on the parameters in the spring-slider model.

[23] As shown in Figure 1, the estimated afterslip distribution significantly overlaps with coseismic slip distributions of the main shock and the largest aftershock inferred by *Miyazaki and Larson* [2008]. This is not consistent with the previous studies of long-term afterslip that show a small amount of overlap between afterslip and main shock regions [*Miyazaki et al.*, 2004; *Ozawa et al.*, 2004; *Baba et al.*, 2006]. In addition, afterslip has a larger strike-slip component than the relative plate motion. We do not think that the estimated afterslip distribution is very reliable for the following reasons. First, cumulative postseismic displace-

Table 1. Fault Parameters for Cumulative Afterslip for the First 5 Hours Following the 2003 Tokachi-oki Earthquake[a]

Latitude (°N)	Longitude (°E)	D (km)	W (km)	L (km)	ϕ (°)	δ (°)
41.800	145.430	10.0	240.0	250.0	240.0	20.0

[a]Latitude and longitude are positions of the upper left edge, D is depth of the upper edge, W is width, L is length, ϕ is strike measured clockwise from north, and δ is dip angle of the fault plane.

Table 2. Values of $\Delta\tau$, $\Delta\tau_{\mathrm{aft}}$, and V_0^- Employed in Inversions Illustrated in Figures 10–12 and 14[a]

Case	$\Delta\tau$ (MPa)	$\Delta\tau_{\mathrm{aft}}$ (MPa)	V_0^- (m/a)
1	1.0	0.08	0.01
2	2.0	0.08	0.01
3	3.0	0.08	0.01
4	1.0	0.08	0.04
5	2.0	0.08	0.04
6	3.0	0.08	0.04
7	1.0	0.08	0.08
8	2.0	0.08	0.08
9	3.0	0.08	0.08
10	2.0	0.00	0.04
11	2.0	0.20	0.04
12	2.0	0.40	0.04

[a]Results for Case 5 is also shown in Figures 7 and 8.

ments for the first 5 hours are less than 1 cm except for the five stations shown in Figure 1, and thus it is difficult to precisely constrain the spatial distribution offshore. Secondly, afterslip distribution is sensitive to the smoothing parameter β^2 in equation (12). If β^2 is significantly smaller than the value used in Figure 1, the main afterslip region becomes smaller and cumulative slip becomes larger, resulting in less overlap between afterslip and main shock slip, although the slip distribution becomes rougher. These limitations make it difficult to obtain a reliable spatial distribution of afterslip. Therefore we regard the afterslip distribution simply as a means to convert slip of the slider into surface displacements and we will not further discuss its spatial distribution. Instead, we focus on its temporal variation which is well captured by the GPS data. We will later show that the assumed spatial distribution of slip does not significantly change the inversion results for friction parameters.

2.2.5. Coseismic Stress Changes and Pre-Earthquake Slip Rate

[24] The governing equations (2) and (5) and initial conditions (6)–(9) indicate that the time evolution of afterslip, $f(t)$, is completely determined by specifying the parameters D_c, $a\sigma$, $b\sigma$, k, V_∞, coseismic stress change due to the main shock, $\Delta\tau$, and the largest aftershock, $\Delta\tau_{\mathrm{aft}}$, and slip velocity before the main shock, V_0^-. It is reasonable to equate V_0^- to the loading velocity V_∞ because of the steady state assumption before the earthquake. Therefore the parameters which affect afterslip evolution $f(t)$ are D_c, $a\sigma$, $b\sigma$, k, V_0^-, $\Delta\tau$, and $\Delta\tau_{\mathrm{aft}}$. Let $\mathbf{m}$ be a vector of parameters to be estimated in the inversion described in section 3

$$\mathbf{m} = [D_c \; a\sigma \; (a-b)\sigma \; k]^T, \tag{14}$$

where we include $(a - b)\sigma$ in $\mathbf{m}$ instead of $b\sigma$. In the inversion method described below, we estimate $\mathbf{m}$ assuming V_0^-, $\Delta\tau$, and $\Delta\tau_{\mathrm{aft}}$ are given.

[25] To estimate $\Delta\tau$ and $\Delta\tau_{\mathrm{aft}}$, we invert coseismic displacements obtained by *Larson and Miyazaki* [2008] for slip distributions of the main shock and the largest aftershock assuming a homogeneous elastic half-space [*Okada*, 1985] employing a Bayesian slip inversion method that is equivalent to minimizing the objective function (12) [*Yabuki and Matsu'ura*, 1992]. Constraints on slip direction are not employed in the inversions. The weighting parameter β^2 is determined by minimizing Akaike's Bayesian information criterion (ABIC) [*Akaike*, 1980; *Yabuki and Matsu'ura*, 1992]. We then calculate the distribution of shear stress change on the plate interface caused by the two earthquakes using the analytical expressions given by *Okada* [1992] with a shear modulus of 3.0×10^4 MPa and a Poisson's ratio of 0.25. Maximum shear stress increase in the direction of afterslip is 2.35 MPa for the main shock and 0.09 MPa for the largest aftershock. Using these estimates as a guide, we estimate $\mathbf{m}$ for several different $\Delta\tau$ and $\Delta\tau_{\mathrm{aft}}$ values in section 4 to examine effects of $\Delta\tau$ and $\Delta\tau_{\mathrm{aft}}$ on estimates of $\mathbf{m}$.

[26] It is difficult to precisely estimate pre-earthquake slip rate of the afterslip zone, V_0^-, because it is located offshore and thus the GEONET network does not provide high enough resolution. We therefore estimate $\mathbf{m}$ for several extreme V_0^- values. Because V_0^- must be equal to or smaller than the rate of the Pacific plate subduction, 0.08 m/a [*DeMets et al.*, 1994], we estimate $\mathbf{m}$ for V_0^- = 0.01, 0.04, and 0.08 m/a. In section 4, we conduct inversions to estimate $\mathbf{m}$ for several different combinations of $\Delta\tau$, $\Delta\tau_{\mathrm{aft}}$, aft, and V_0^- values which are listed in Table 2.

3. Inversion Method

3.1. Probabilistic Formulation

[27] We formulate an inversion method for estimating $\mathbf{m}$ within a probabilistic, Bayesian, framework [e.g., *MacKay*, 2003]. Bayes' theorem states that the posterior probability density function (PDF) of model parameters, $\mathbf{m}$, given data, $\mathbf{d}$, $p(\mathbf{m}|\mathbf{d})$, is

$$p(\mathbf{m}|\mathbf{d}) = \frac{p(\mathbf{d}|\mathbf{m})p(\mathbf{m})}{\int_{-\infty}^{\infty} p(\mathbf{d}|\mathbf{m})p(\mathbf{m})d\mathbf{m}}, \tag{15}$$

where $p(\mathbf{d}|\mathbf{m})$ is the PDF of data given the model parameters, which accounts for the theoretical data-parameter relationship, $p(\mathbf{m})$ is the prior PDF of the model parameters, and the denominator is a constant that normalizes $p(\mathbf{m}|\mathbf{d})$ and is independent of $\mathbf{m}$.

[28] We relate the model parameter $\mathbf{m}$ to observed data $\mathbf{d}$ by the observation equation

$$\mathbf{d} = \mathbf{g}(\mathbf{m}) + \mathbf{e}, \tag{16}$$

where $\mathbf{g}(\mathbf{m})$ represents model-predicted displacements at the GPS stations and is computed from equation (13). $\mathbf{e}$ is an error vector that is assumed to follow a Gaussian distribution of mean $\mathbf{0}$ and covariance matrix Σ_d. Equation (16) indicates that the probability density of $\mathbf{d}$ given $\mathbf{m}$, $p(\mathbf{d}|\mathbf{m})$, follows a Gaussian distribution of mean $\mathbf{g}(\mathbf{m})$ and covariance matrix Σ_d

$$p(\mathbf{d}|\mathbf{m}) = (2\pi)^{-N/2}|\boldsymbol{\Sigma}_d|^{-1/2} \cdot \exp\left\{-\frac{1}{2}[\mathbf{d}-\mathbf{g}(\mathbf{m})]^T\boldsymbol{\Sigma}_d^{-1}[\mathbf{d}-\mathbf{g}(\mathbf{m})]\right\}, \tag{17}$$

where N is the dimension of $\mathbf{d}$.

[29] We assume that we have no prior knowledge about the model parameters except that D_c, $a\sigma$, $b\sigma$, and k are

positive. We express this prior information as the prior PDF, $p(\mathbf{m})$, by assuming that $p(\mathbf{m})$ takes a uniform nonzero value when the above conditions are satisfied, and takes zero otherwise.

[30] Substituting $p(\mathbf{d}|\mathbf{m})$ and $p(\mathbf{m})$ into Bayes' theorem (equation (15)), we obtain the posterior PDF $p(\mathbf{m}|\mathbf{d})$ that is proportional to $p(\mathbf{d}|\mathbf{m})$ (equation (17)) when D_c, $a\sigma$, $b\sigma$, and k are positive and is equal to zero otherwise

$$p(\mathbf{m}|\mathbf{d}) = \begin{cases} c\exp\left\{-\frac{1}{2}[\mathbf{d}-\mathbf{g}(\mathbf{m})]^T\boldsymbol{\Sigma}_d^{-1}[\mathbf{d}-\mathbf{g}(\mathbf{m})]\right\} & \text{for } D_c>0, a\sigma>0, b\sigma>0, k>0 \\ 0 & \text{otherwise} \end{cases}, \tag{18}$$

where c is a constant that is introduced to normalize $p(\mathbf{m}|\mathbf{d})$ (i.e., $\int_{-\infty}^{\infty} p(\mathbf{m}|\mathbf{d})d\mathbf{m} = 1$) and is independent of $\mathbf{m}$. This posterior PDF of $\mathbf{m}$, $p(\mathbf{m}|\mathbf{d})$, is the solution to the inverse problem.

[31] Because the function $\mathbf{g}(\mathbf{m})$ in the observation equation (16) is nonlinear and does not have closed-form analytical expressions, and because the posterior PDF, $p(\mathbf{m}|\mathbf{d})$, given by (18) has a non-Gaussian distribution, it is not possible to obtain the posterior PDF analytically. Thus we numerically construct a discrete representation of the posterior PDF by generating many samples from the PDF using the Metropolis algorithm which is one of the common Markov chain Monte Carlo (MCMC) methods [e.g., *Metropolis et al.*, 1953; *Hastings*, 1970; *Gamerman*, 1997; *MacKay*, 2003].

3.2. Estimating the Posterior Distribution

[32] In Appendix A, we illustrate the Metropolis algorithm that generates samples from the posterior PDF, $p(\mathbf{m}|\mathbf{d})$, given by equation (18). Let us assume that we have a set of N_s samples of $\mathbf{m}$, $\{\mathbf{m}_1, \mathbf{m}_2, \ldots, \mathbf{m}_{Ns}\}$ that can be regarded as a set of independent samples drawn from the posterior PDF, $p(\mathbf{m}|\mathbf{d})$. This is equivalent to approximating the posterior PDF with the samples as follows

$$p(\mathbf{m}|\mathbf{d}) \cong \frac{1}{N_s}\sum_{i=1}^{N_s}\delta(\mathbf{m}-\mathbf{m}_i), \tag{19}$$

where $\delta(\mathbf{m})$ is the Dirac delta function. Let us denote a sample $\mathbf{m}_i$ as $[D_{ci}\ a\sigma_i\ (a-b)\sigma_i\ k_i]^T$. In this notation, the posterior PDF (equation (19)) is expressed as

$$p(D_c, a\sigma, (a-b)\sigma, k|\mathbf{d}) \cong \frac{1}{N_s}\sum_{i=1}^{N_s}\delta(D_c-D_{ci})\delta(a\sigma-a\sigma_i) \cdot \delta[(a-b)\sigma-(a-b)\sigma_i]\delta(k-k_i). \tag{20}$$

The marginal posterior PDF of D_c, $p(D_c|\mathbf{d})$, is obtained by integrating equation (20) with respect to $a\sigma$, $(a-b)\sigma$, and k

$$p(D_c|\mathbf{d}) = \int_{-\infty}^{\infty}\int_{-\infty}^{\infty}\int_{-\infty}^{\infty} p(D_c, a\sigma, (a-b)\sigma, k|\mathbf{d})\mathrm{d}a\sigma\mathrm{d}(a-b)\sigma\mathrm{d}k \cong \frac{1}{N_s}\sum_{i=1}^{N_s}\delta(D_c-D_{ci}). \tag{21}$$

Equation (21) indicates that the marginal posterior PDF of D_c, $p(D_c|\mathbf{d})$, is expressed by the set of samples $\{D_{c1}, D_{c2}, \ldots, D_{cNs}\}$. The marginal posterior PDFs of $a\sigma$, $(a-b)\sigma$, and k expressed by samples are obtained similarly. We can obtain α % confidence interval for D_c by sorting the samples $\{D_{c1}, D_{c2}, \ldots, D_{cNs}\}$ in ascending order and then discarding the top and bottom $(100-\alpha)/2$% of the sorted samples. The confidence intervals for the other parameters are obtained similarly.

[33] The posterior probability that D_c takes a value between d and $d+\Delta d$, $P(d \le D_c \le d+\Delta d|\mathbf{d})$, is obtained by

$$P(d \le D_c \le d+\Delta d|\mathbf{d}) = \int_d^{d+\Delta d} p(D_c|\mathbf{d})\mathrm{d}D_c \cong \frac{1}{N_s}(\text{number of samples with } d \le D_{ci} \le d+\Delta d). \tag{22}$$

Thus the marginal posterior probability distribution of D_c is obtained from equation (22). The value of D_c that maximizes the marginal posterior probability distribution can be considered to be the most probable or the optimal estimate of D_c. The marginal posterior probability distributions and the optimal estimates of $a\sigma$, $(a-b)\sigma$, and k are obtained similarly.

4. Results

[34] As described in section 2.2.5, we conduct inversions for estimating $\mathbf{m}$ with several different values of coseismic stress changes due to the main shock, $\Delta\tau$, and the largest aftershock, $\Delta\tau_{\text{aft}}$, and pre-earthquake slip velocity, V_0^-. Values of $\Delta\tau$, $\Delta\tau_{\text{aft}}$, and V_0^- in each inversion are listed in Table 2. In section 4.1, we show the results obtained from the inversion with $\Delta\tau$ = 2.0 MPa, $\Delta\tau_{\text{aft}}$ = 0.08 MPa, and V_0^- = 0.04 m/a (Case 5 in Table 2) as a representative case. We then discuss effects of $\Delta\tau$, $\Delta\tau_{\text{aft}}$, and V_0^- on estimate of $\mathbf{m}$ in section 4.2.

4.1. Fixed $\Delta\tau$, $\Delta\tau_{\text{aft}}$, and V_0^-

[35] Figure 7 shows joint posterior distributions of the Monte Carlo samples generated by the MCMC method for Case 5 in Table 2 ($\Delta\tau$ = 2.0 MPa, $\Delta\tau_{\text{aft}}$ = 0.08 MPa, V_0^- = 0.04 m/a), which represent the posterior PDF, $p(\mathbf{m}|\mathbf{d})$. The sample distributions show strong correlations between D_c and $a\sigma$ and between $(a-b)\sigma$ and k. These correlations indicate strong tradeoffs exist between D_c and $a\sigma$ and between $(a-b)\sigma$ and k. We will discuss these correlations later in this section. Figure 2 shows the model-predicted surface displacements together with the observed GPS time series, indicating that the model fits the GPS data largely within the 2σ uncertainties.

[36] Figure 8 shows the marginal posterior probability distributions of the model parameters computed from $p(\mathbf{m}|\mathbf{d})$ and 95% confidence intervals for Case 5 in Table 2 ($\Delta\tau$ = 2.0 MPa, $\Delta\tau_{\text{aft}}$ = 0.08 MPa, V_0^- = 0.04 m/a). The estimated 95% confidence interval of D_c is 2.6×10^{-4} to

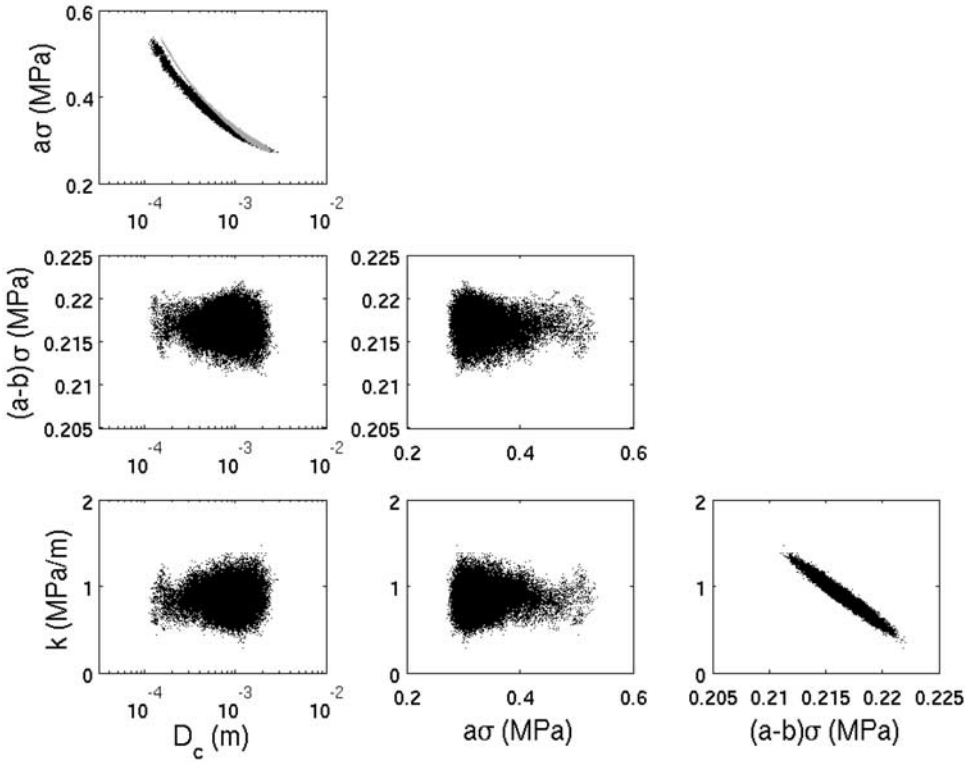

Figure 7. Distributions of Monte Carlo samples (black dots) that represent the posterior PDF of $\mathbf{m} = [D_c \quad a\sigma \quad (a-b)\sigma \quad k]^T$, $p(\mathbf{m}|\mathbf{d})$, for Case 5 in Table 2. Gray dots represent D_c values predicted from equation (11) using $a\sigma$, $b\sigma$, and t_{max} values for the Monte Carlo samples and $\Delta\tau$ and V_0^- values assumed in Case 5.

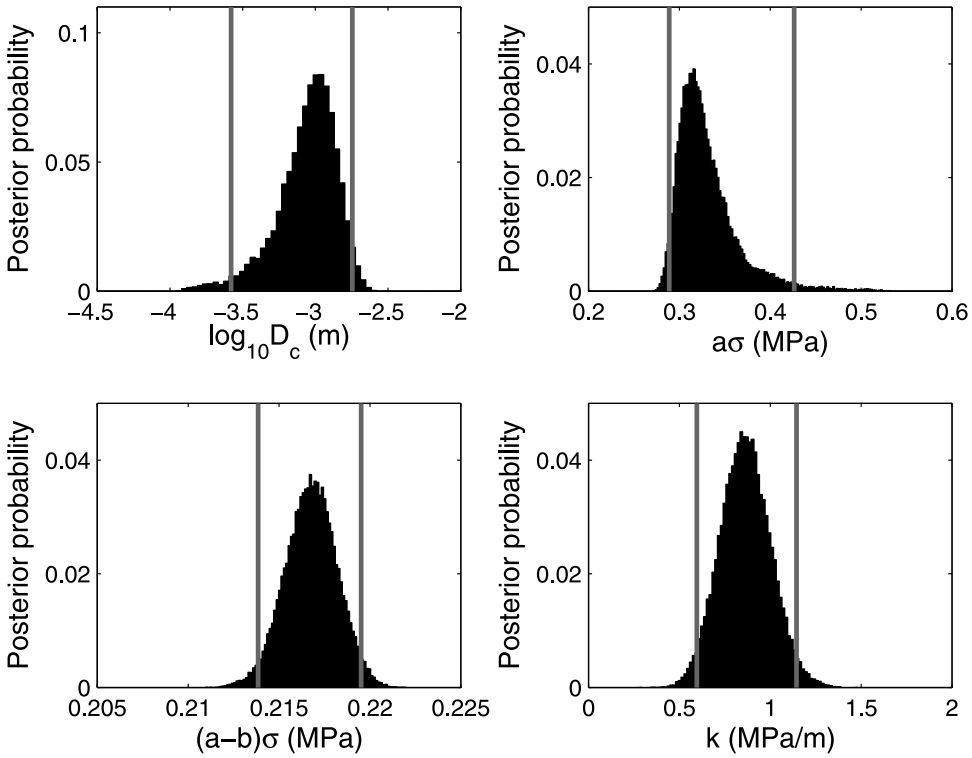

Figure 8. Marginal posterior probability distributions of D_c, $a\sigma$, $(a-b)\sigma$, and k computed from the Monte Carlo samples that represent the posterior PDF, $p(\mathbf{m}|\mathbf{d})$, shown in Figure 7. Gray vertical lines denote 95% confidence intervals.

1.8×10^{-3} m with the most probable value of 1.1×10^{-3} m (Figure 8). This value is 10 to 10^3 times larger than typical laboratory values of 10^{-6} to 10^{-4} m [e.g., *Marone*, 1998; *Paterson and Wong*, 2005]. The estimated range is consistent with the estimate $D_c \sim 10^{-3}$ m by *Marone and Kilgore* [1993] for a gouge zone of thickness 10 cm which is inferred for an exhumed section of the southern San Andreas fault system.

[37] The 95% confidence interval of $a\sigma$ is 0.29 to 0.43 MPa with the most probable value of 0.32 MPa (Figure 8). The depth of the afterslip zone shown in Figure 1 is about 20–40 km. The effective normal stress in this depth range is 350–700 MPa assuming a lithostatic load and hydrostatic pore pressure. Combining the estimated range of $a\sigma$ with the effective normal stress of 350–700 MPa, we obtain $a \simeq 4.1 \times 10^{-4}$–$1.2 \times 10^{-3}$. These values are 1 to 2 orders of magnitude smaller than laboratory-measured values for wet granite gouge with temperatures up to 600°C, $a = 8.0 \times 10^{-3}$–1.2×10^{-1} [*Blanpied et al.*, 1998]. Alternatively, if we assume a is in the laboratory range, $a = 8.0 \times 10^{-3}$–1.2×10^{-1}, combining this range with the estimated range of $a\sigma$ yields the effective normal stress of $\sigma \simeq 2$–53 MPa. These values are 1 to 2 orders of magnitude smaller than the range 350–700 MPa in which the hydrostatic pore pressure is assumed. Therefore the estimated range of $a\sigma$ indicates that a is smaller than typical laboratory values and/or the pore pressure on the plate boundary is significantly elevated above the hydrostatic value. Numerical simulations of aseismic slip transients by *Liu and Rice* [2007] also suggest elevated pore pressure. They showed that simulations with near-lithostatic pore pressure can produce slip transients with recurrence intervals of about 1 year which are consistent with observed slip transients in the Cascadia subduction zone and cannot be simulated in their previous study [*Liu and Rice*, 2005] that employs effective normal stress of 50–100 MPa.

[38] The 95% confidence interval of $(a - b)\sigma$ is 0.214 to 0.220 MPa (Figure 8). $(a - b)\sigma$ has been estimated from afterslip of other large earthquakes with mechanical models of afterslip using the velocity strengthening friction law (equation (3)); $(a - b)\sigma$ was estimated as 0.4 MPa for the 1999 Izmit earthquake [*Hearn et al.*, 2002], 0.34–1.5 MPa for the 1999 Chi-Chi earthquake [*Perfettini and Avouac*, 2004], 0.26 MPa for the 2001 Peru earthquake [*Perfettini et al.*, 2005], 0.48–0.53 MPa for the 1992 Landers earthquake [*Perfettini and Avouac*, 2007], 0.2–0.7 MPa for the 2005 Nias-Simeulue, Sumatra, earthquake [*Hsu et al.*, 2006], and 0.5 MPa for the 2002 Denali, Alaska, earthquake [*Johnson et al.*, 2009]. The range of $(a - b)\sigma$ estimated from our inversion is roughly consistent with these previous estimates and is close to the estimates for the Peru and the Nias-Simeulue earthquakes which are subduction earthquakes. *Miyazaki et al.* [2006] examined the relation between evolution of shear stress change and time variation of afterslip velocity following the 2003 Tokachi-oki earthquake based on their result of kinematic slip inversion. *Miyazaki et al.* [2006] found that the relation was consistent with the velocity strengthening friction law (equation (3)) and inferred $(a - b)\sigma$ as ~0.2 MPa. *Hsu et al.* [2006] also estimated $(a - b)\sigma$ in the same manner as *Miyazaki et al.* [2006] and found $(a - b)\sigma$ to be ~0.2 MPa. Our result is also close to their estimate. On the other hand, our estimate is an order of magnitude larger than estimates from a rate-state model of afterslip following the 2004 Parkfield earthquake [*Johnson et al.*, 2006].

[39] If we assume that the effective normal stress σ is given by lithostatic pressure minus hydrostatic pore pressure, σ is 350–700 MPa as described previously and we obtain $a - b$ of 3.1×10^{-4}–6.3×10^{-4}. These values are 1 to 2 orders of magnitude smaller than laboratory-measured values for wet granite gouge with temperatures up to 600°C, which are in the range $a - b \simeq 5 \times 10^{-3}$–$5 \times 10^{-2}$ [*Blanpied et al.*, 1995]. Alternatively, if we assume $a - b$ is in the laboratory range, we obtain $\sigma \sim 4$–44 MPa, again suggesting that the pore pressure is significantly elevated above the hydrostatic value.

[40] The 95% confidence interval of the spring stiffness k is 0.60 to 1.14 MPa/m (Figure 8). The relationship between the stiffness and radius r of a circular crack in an elastic medium of rigidity G is given by [e.g., *Dieterich*, 1986]

$$k = \frac{7\pi G}{24r}. \tag{23}$$

From this relationship, the estimated range for k corresponds to a patch radius of 24 to 46 km, which is smaller than or equal to the radius of the inferred slip patch shown in Figure 1.

[41] We now examine the strong tradeoffs between D_c and $a\sigma$ and between $(a - b)\sigma$ and k shown in Figure 7. The theoretical study conducted by *Perfettini and Ampuero* [2008] that was described in section 2.2.3 and the numerical simulations shown in section 2.2.3 (Figures 5a and 5b) suggest that the tradeoff between D_c and $a\sigma$ can be explained by the timing of the rapid acceleration of afterslip. To verify this idea, we calculate D_c from equation (11) for each Monte Carlo sample using $a\sigma$ and $b\sigma$ values for each sample obtained in the inversion, $\Delta\tau$ and V_0^- assumed in the inversion, and t_{max} obtained from the slip velocity history for each sample. The top left plot in Figure 7 shows the predicted D_c values (gray dots) together with the Monte Carlo samples obtained in the inversion (black dots). The strong tradeoff derived from the inversion is well predicted by equation (11). This indicates that D_c and $a\sigma$ are largely constrained by the timing of the rapid acceleration.

[42] *Perfettini and Ampuero* [2008] showed that, in a rate-and-state model of afterslip with initial conditions similar to equations (6) and (7), slip decelerates according the steady state velocity strengthening friction (equation (3)) after the time of the maximum velocity t_{max} if k is sufficiently smaller than $b\sigma/D_c$. They showed that slip evolution for $t > t_{max}$ can be described by an analytical solution for afterslip governed by equation (3) [*Perfettini and Avouac*, 2004]

$$s(t') = \frac{(a-b)\sigma}{k} \ln\left[1 + \frac{V_{max}}{V_\infty}\left(e^{t'/t_r} - 1\right)\right] \tag{24}$$

where $t' = t - t_{max}$, $t_r = (a - b)\sigma/kV_\infty$, and V_{max} is given by equation (10). We find that equation (24) gives an explanation for the tradeoff between $(a - b)\sigma$ and k. To show this, we calculate the sum of squared residuals between slip history for $t > t_{max}$ computed from the optimal values of the model parameters obtained in the inversion and sampled every 1 minute and slip history computed from

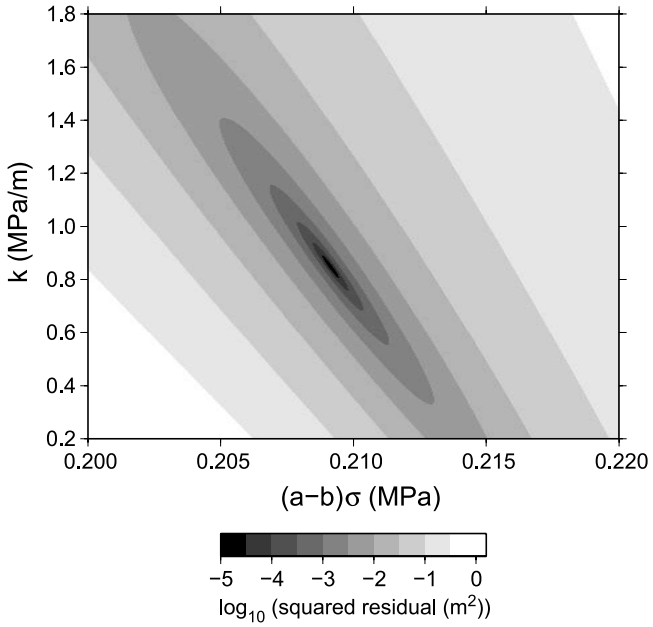

Figure 9. Sum of squared residuals between slip history for the deceleration phase ($t > t_{max}$) computed from the optimal values of the model parameters obtained for Case 5 in Table 2 and slip history computed from equation (24) as a function of $(a - b)\sigma$ and k.

equation (24). We calculate the sum of squared residuals for ranges of values of $(a - b)\sigma$ and k in equation (24). Figure 9 shows the sum of squared residuals as a function of $(a - b)\sigma$ and k in equation (24), indicating strong negative correlation between $(a - b)\sigma$ and k which is similar to the correlation shown in Figure 7. The region of small residuals in Figure 9 is slightly different from the high probability region in Figure 7. This is because the largest aftershock is modeled in the inversion, whereas it is not taken into consideration in the analytical solution given by equation (24). However, the analytical solution can reproduce the slip history derived from the inversion almost perfectly with $(a - b)\sigma$ and k slightly different from those estimated in the inversion.

[43] The estimates of the model parameters are dependent on the assumed spatial distribution of afterslip (Figure 1) because we relate the spring-slider system to the surface displacements using equation (13). To check whether the assumed spatial distribution has a significant effect on the inversion results, we apply the inversion method assuming slip distributions with diffrerent roughnesses. These are obtained with β^2 between 10^{-3} and 1 where β^2 is the smoothing parameter in equation (12). Note that $\beta^2 = 0.05$ was used to obtain the slip distribution shown in Figure 1. The slip distribution with $\beta^2 = 1$ is much smoother than that shown in Figure 1 and has only a single large slip patch with a maximum slip of 9.6 cm. This slip distribution cannot fit the data well because it is too smooth. The slip distribution with $\beta^2 = 10^{-3}$ is much rougher and the maximum slip is 36.2 cm. This slip distribution has multiple slip patches and is thus inconsistent with the spring-slider assumption. Therefore these two slip distributions can be regarded as extreme cases. The 95% confidence regions for the model parameters for β^2 between 10^{-3} and 1 fall within $2.4 \times 10^{-4} \leq D_c \leq 3.6 \times 10^{-3}$ m, $0.26 \leq a\sigma \leq 0.44$ MPa, $0.20 \leq (a - b)\sigma \leq 0.23$ MPa, and $0.27 \leq k \leq 1.88$ MPa/m. The estimated ranges are not considerably different from those estimated with the slip distribution shown in Figure 1 even if the extremely smooth or rough slip distribution is employed. This indicates that estimates of the model parameters are rather insensitive to the assumed slip distribution and suggests that the model parameters are largely constrained by the temporal pattern of the data.

4.2. Effect of Varying $\Delta\tau$, $\Delta\tau_{aft}$, and V_0^-

[44] We examine effects of $\Delta\tau$ and V_0^-, which are fixed in the inversion shown in Figures 7 and 8, on estimates of the model parameters. For this purpose, we estimate the posterior PDFs $p(\mathbf{m}|\mathbf{d})$ for Cases 1–9 in Table 2, each of which has different $\Delta\tau$ and V_0^- values. Figures 10, 11, and 12 show the marginal posterior probability distributions of D_c, $a\sigma$, $(a - b)\sigma$, and k for $V_0^- = 0.01$, 0.04, and 0.08 m/a, respectively, and each figure shows the marginal distributions for $\Delta\tau = 1.0$, 2.0, and 3.0 MPa. In all the cases shown in Figures 10–12, $\Delta\tau_{aft}$ is fixed to 0.08 MPa. Figures 10–12 show that the marginal posterior probability distributions of D_c are similar for all the cases, indicating that $\Delta\tau$ and V_0^- do not significantly affect estimates of D_c. On the other hand, estimates of $a\sigma$, $(a - b)\sigma$ and k are positively correlated with $\Delta\tau$ (Figures 10–12). $a\sigma$, $(a - b)\sigma$ and k are also positively correlated with V_0^- although their dependencies on V_0^- are weaker than those on $\Delta\tau$. Figure 13 shows slip histories computed from the optimal values of D_c, $a\sigma$, $(a - b)\sigma$ and k which maximize the marginal posterior probability distributions shown in Figures 10–12, indicating that all the cases generate similar slip histories. This indicates that it is difficult to discriminate the 9 cases from the GPS time series. Therefore uncertainties in $a\sigma$, $(a - b)\sigma$, and k becomes significantly larger if uncertainties in $\Delta\tau$ and V_0^- are taken into consideration. If $\Delta\tau$ is between 1.0 and 3.0 MPa and V_0^- is between 0.01 and 0.08 m/a, combining the 95% confidence intervals for all the cases shown in Figures 10–12 yields approximate ranges of $a\sigma$, $(a - b)\sigma$, and k, $a\sigma \simeq 0.12$–0.64 MPa, $(a - b)\sigma \simeq 0.097$–$0.351$ MPa, and $k \simeq 0.28$–1.84 MPa/m, in which uncertainties in $\Delta\tau$ and V_0^- are taken into consideration.

[45] We next examine effects of stress change caused by the largest aftershock, $\Delta\tau_{aft}$, on estimates of the model parameters. For this purpose, we conduct inversions to estimate the posterior PDFs of $\mathbf{m}$, $p(\mathbf{m}|\mathbf{d})$, for Cases 10–12 in Table 2. In these cases, different values of $\Delta\tau_{aft}$, $\Delta\tau_{aft} =$ 0.0, 0.2, and 0.4 MPa are employed, whereas $\Delta\tau$ and V_0^- are fixed to 2.0 MPa and 0.04 m/a, respectively, which are the same values as Case 5 whose results are shown in Figures 7 and 8. Figure 14 shows the marginal posterior probability distributions of D_c, $a\sigma$, $(a - b)\sigma$, and k for Cases 5 and 10–12. Figure 14 shows that as $\Delta\tau_{aft}$ increases the marginal posterior probability distributions of D_c are shifted toward smaller values and becomes broader. The marginal posterior probability distributions of $a\sigma$ are weakly negatively correlated with $\Delta\tau_{aft}$, whereas those of $(a - b)\sigma$ and k are strongly positively correlated with $\Delta\tau_{aft}$. Figure 15a shows slip histories computed from the optimal values of D_c, $a\sigma$, $(a - b)\sigma$ and k which maximize the marginal posterior probability distributions shown in

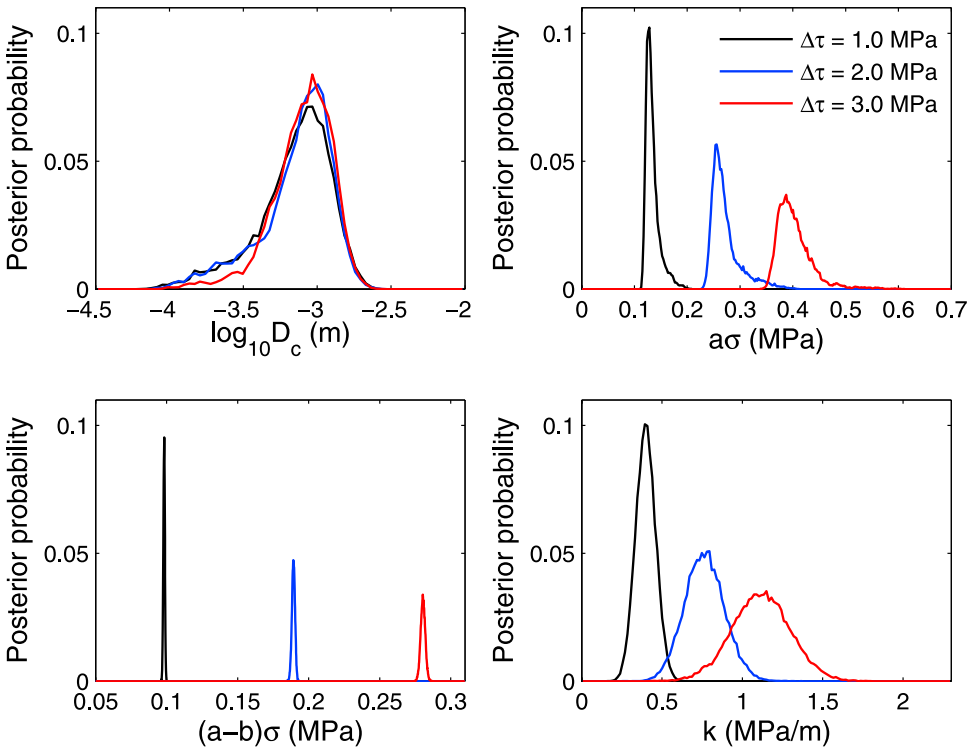

Figure 10. Marginal posterior probability distributions of D_c, $a\sigma$, $(a - b)\sigma$, and k for Cases 1 ($\Delta\tau$ = 1.0 MPa, black curve), 2 ($\Delta\tau$ = 2.0 MPa, blue curve), and 3 ($\Delta\tau$ = 3.0 MPa, red curve) in Table 2. In all the cases, pre-earthquake slip velocity, V_0^-, and stress change due to the largest aftershock, $\Delta\tau_{\text{aft}}$, are fixed to V_0^- = 0.01 m/a and $\Delta\tau_{\text{aft}}$ = 0.08 MPa, respectively.

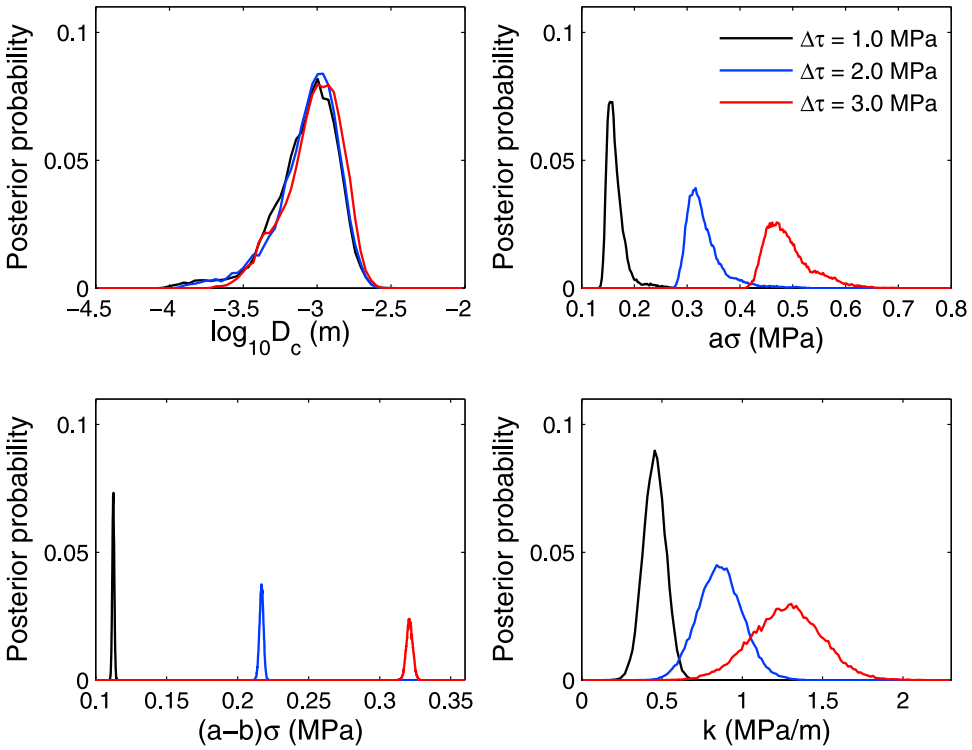

Figure 11. Marginal posterior probability distributions of D_c, $a\sigma$, $(a - b)\sigma$, and k for Cases 4 ($\Delta\tau$ = 1.0 MPa, black curve), 5 ($\Delta\tau$ = 2.0 MPa, blue curve), and 6 ($\Delta\tau$ = 3.0 MPa, red curve) in Table 2. In all the cases, pre-earthquake slip velocity, V_0^-, and stress change due to the largest aftershock, $\Delta\tau_{\text{aft}}$, are fixed to V_0^- = 0.04 m/a and $\Delta\tau_{\text{aft}}$ = 0.08 MPa, respectively.

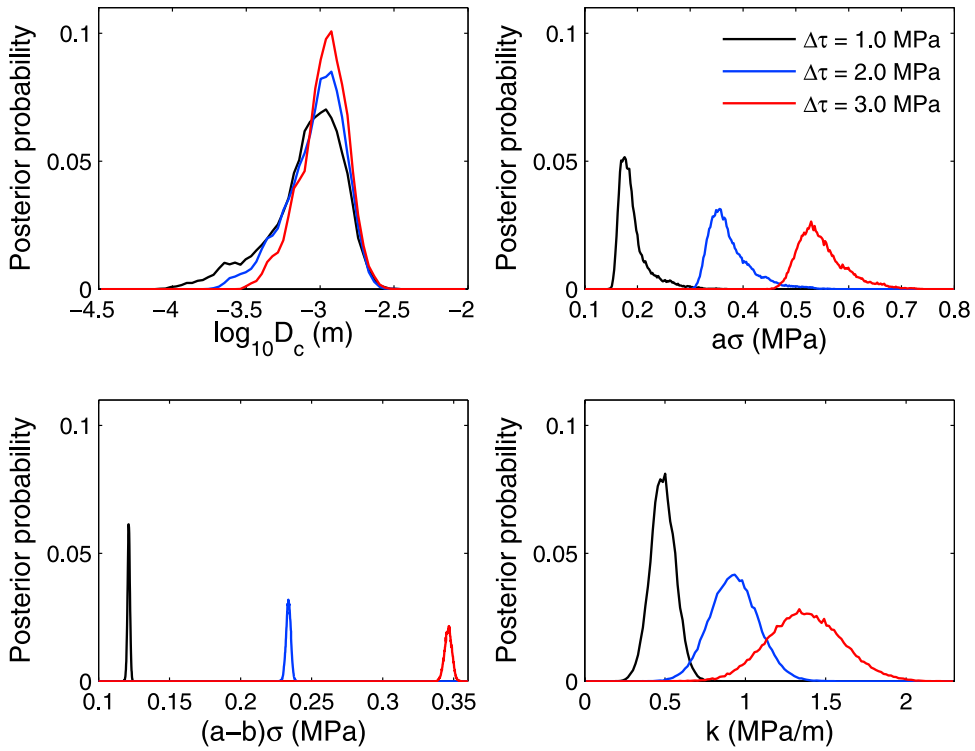

Figure 12. Marginal posterior probability distributions of D_c, $a\sigma$, $(a - b)\sigma$, and k for Cases 7 ($\Delta\tau$ = 1.0 MPa, black curve), 8 ($\Delta\tau$ = 2.0 MPa, blue curve), and 9 ($\Delta\tau$ = 3.0 MPa, red curve) in Table 2. In all the cases, pre-earthquake slip velocity, V_0^-, and stress change due to the largest aftershock, $\Delta\tau_{aft}$, are fixed to V_0^- = 0.08 m/a and $\Delta\tau_{aft}$ = 0.08 MPa, respectively.

Figure 14, indicating that all the cases generate similar slip histories. This indicates that it is difficult to discriminate the 4 cases from the available GPS data. Therefore uncertainties in D_c, $a\sigma$, $(a - b)\sigma$, and k becomes larger if uncertainties in $\Delta\tau_{aft}$ are taken into account.

[46] The estimated ranges of D_c, $a\sigma$, $(a - b)\sigma$, and k for the 12 cases in Table 2 are of the same order as the parameter ranges obtained in section 4.1. Therefore uncertainties in $\Delta\tau$, $\Delta\tau_{aft}$, and V_0^- do not significantly change the comparisons with the laboratory values and the previous geodetic studies discussed in section 4.1.

[47] We now examine contributions of the largest aftershock to afterslip evolution. Figure 15b compares slip velocity histories corresponding to slip histories shown in Figure 15a. For comparison, Figure 16 shows slip and slip velocity histories computed from the same values of D_c, $a\sigma$, $(a - b)\sigma$, k, $\Delta\tau$, and V_0^- as those used in Figure 15 assuming no stress change from the largest aftershock ($\Delta\tau_{aft}$ = 0.00 MPa). For the case with $\Delta\tau_{aft}$ = 0.08 MPa, the largest aftershock occurs during rapid acceleration of afterslip (Figure 15b). The slip velocity history is similar to that for the case with $\Delta\tau_{aft}$ = 0.00 MPa as shown in Figure 15b. Cumulative afterslip for 5 hours following the main shock is 18.1 cm in this case (Figure 15a), whereas it is 13.8 cm if we do not impose $\Delta\tau_{aft}$ (Figure 16a). This indicates that the main shock has a larger effect on afterslip evolution than the largest aftershock in this case. Slip velocity history for the case with $\Delta\tau_{aft}$ = 0.20 MPa shows that the acceleration phase induced by the main shock ends around the time of the largest aftershock and another acceleration phase is triggered by the largest aftershock (Figure 15b). In this case, cumulative afterslip for 5 hours following the main shock is 18.0 cm (Figure 15a), whereas it is 9.7 cm if $\Delta\tau_{aft}$ is not imposed (Figure 16a), indicating that about half of the afterslip is attributed to the stress change from the

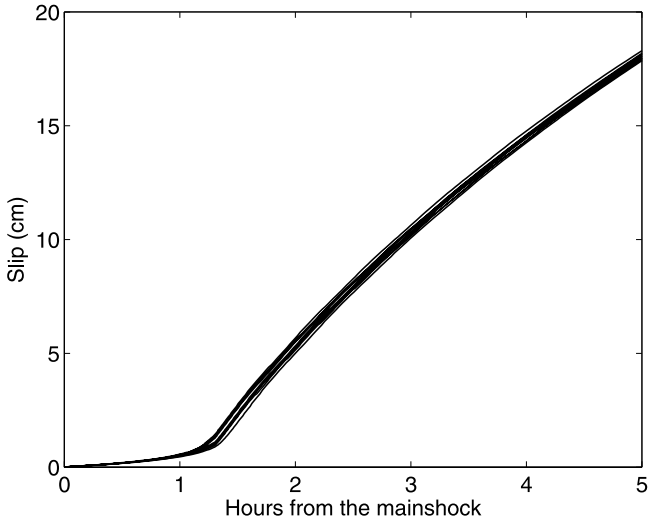

Figure 13. Slip histories computed from the optimal values of D_c, $a\sigma$, $(a - b)\sigma$ and k for Cases 1–9 in Table 2 which have different values of $\Delta\tau$ and V_0^-. The optimal values are defined as the values that maximize the marginal posterior probability distributions shown in Figures 10–12.

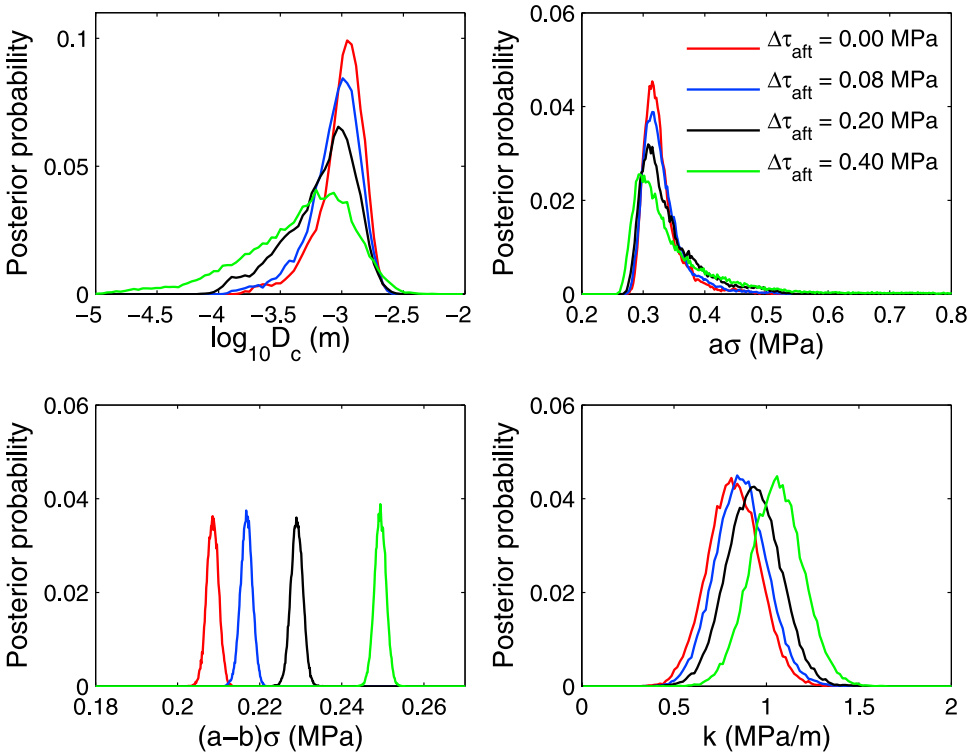

Figure 14. Marginal posterior probability distributions of D_c, $a\sigma$, $(a - b)\sigma$, and k for Cases 10 ($\Delta\tau_{aft}$ = 0.00 MPa, red curve), 5 ($\Delta\tau_{aft}$ = 0.08 MPa, blue curve), 11 ($\Delta\tau_{aft}$ = 0.20 MPa, black curve), and 12 ($\Delta\tau_{aft}$ = 0.40 MPa, green curve) in Table 2. In all the cases, stress change due to the main shock, $\Delta\tau$, and pre-earthquake slip velocity, V_0^-, are fixed to $\Delta\tau$ = 2.0 MPa and V_0^- = 0.04 m/a, respectively.

largest aftershock. For the case $\Delta\tau_{aft}$ = 0.40 MPa, as shown in Figure 15b, the acceleration phase caused by the main shock ends well before the largest aftershock and then slip decelerates slowly until the time of the largest aftershock. Then another short acceleration phase is triggered by the largest aftershock. Cumulative afterslip for the first 5 hours is 18.1 cm (Figure 15a), whereas it is 5.7 cm if we do not impose $\Delta\tau_{aft}$ (Figure 16a). Therefore in this case, 68% of cumulative afterslip for the first 5 hours is contributed by the largest aftershock. Although the four cases generate different slip velocity histories as shown in Figure 15b, corresponding slip histories shown in Figure 15a are quite

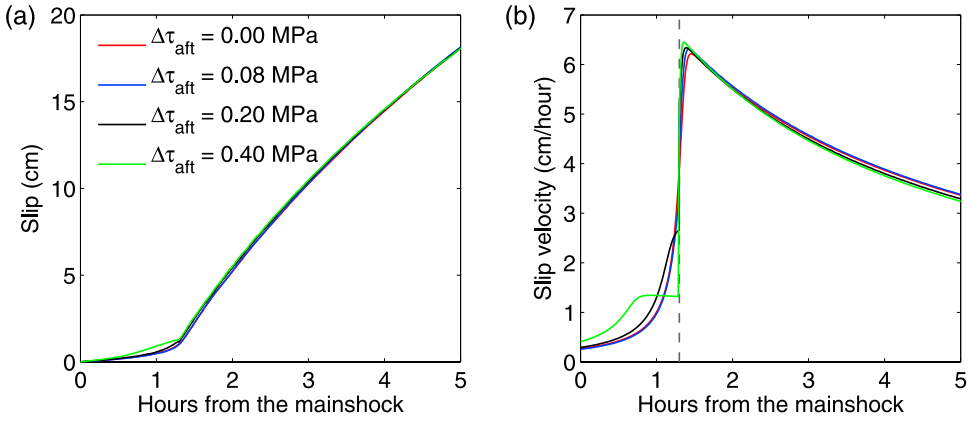

Figure 15. (a) Slip histories computed from the optimal values of D_c, $a\sigma$, $(a - b)\sigma$, and k for Cases 5 and 10–12 in Table 2 which have different values of $\Delta\tau_{aft}$. Red, blue, black, and green curves correspond to Cases 10 ($\Delta\tau_{aft}$ = 0.00 MPa), 5 ($\Delta\tau_{aft}$ = 0.08 MPa), 11 ($\Delta\tau_{aft}$ = 0.20 MPa), and 12 ($\Delta\tau_{aft}$ = 0.40 MPa), respectively. The optimal values are defined as the values that maximize the marginal posterior probability distributions shown in Figure 14. In all the cases, stress change due to the main shock, $\Delta\tau$, and pre-earthquake slip velocity, V_0^-, are fixed to $\Delta\tau$ = 2.0 MPa and V_0^- = 0.04 m/a, respectively. (b) Slip velocity histories corresponding to slip histories shown in Figure 15a. Vertical dashed line denotes time of the largest aftershock.

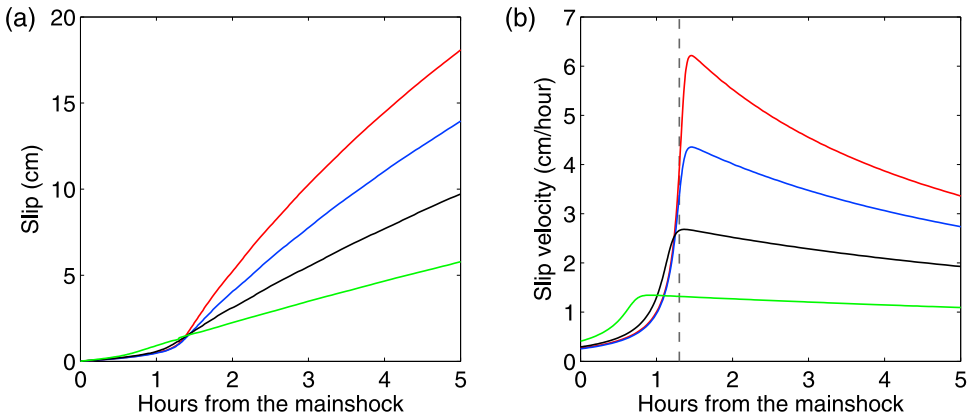

Figure 16. (a) Slip histories computed from the optimal values of D_c, $a\sigma$, $(a - b)\sigma$, and k for Cases 5 and 10–12 in Table 2, which are the same as those used in Figure 15, assuming no stress change from the largest aftershock ($\Delta\tau_{aft} = 0.00$ MPa). Values of $\Delta\tau$, and V_0^- are also the same as those used in Figure 15 ($\Delta\tau = 2.0$ MPa, $V_0^- = 0.04$ m/a). Red, blue, black, and green curves correspond to those shown in Figure 15. (b) Slip velocity histories corresponding to slip histories shown in Figure 16a. Vertical dashed line denotes time of the largest aftershock.

similar to each other. Therefore it is difficult to determine the relative contributions of the main shock and the largest aftershock to afterslip evolution from the available GPS data.

[48] As described in section 2.2.3, a large D_c value delays rapid acceleration of afterslip. However, we find that, in the case of $\Delta\tau = 2.0$ MPa and $V_0^- = 0.04$ m/a, if $\Delta\tau_{aft}$ is larger than 0.5 MPa, arbitrarily large D_c values can fit rapid acceleration of surface displacements immediately after the largest aftershock and therefore D_c cannot be constrained by the GPS data. However, this threshold value is about a factor of 6 larger than the value of $\Delta\tau_{aft}$ estimated in section 2.2.5.

5. Discussion

[49] In the Results section, we thoroughly examined the third question we raised in the Introduction, "What friction parameters are consistent with the observations?" The inferred friction parameters are, of course, dependent on model assumptions and the ability of the model to fit the data, and therefore should be viewed with caution. Although the general patterns of the early postseismic deformation are reproduced by the forward model (Figure 2), the model relies on some strong assumptions. First, the afterslip patch is modeled by a zero-dimensional spring-slider system which neglects spatial variations in friction parameters, stress, state, and slip velocity. Second, the spring stiffness k is assumed not to vary with time. Because k is a function of the patch size (equation (23)) [*Dieterich*, 1986], this is equivalent to assuming that the patch size does not vary with time, although in reality the size of the afterslip zone must expand with time. By focusing on only the first 5 hours of the postseismic period, we have attempted to minimize the effect of an expanding slip patch on our parameter inferences. Similarly, we compute model-predicted surface displacements using equation (13) which assumes that spatial pattern of afterslip distribution does not vary with time. These assumptions may be problematic because, for example, *Miyazaki and Larson* [2008] inferred downdip propagation of afterslip in the first 4 hours following the main shock from a time-dependent kinematic slip inversion, although it is difficult to resolve the spatial distribution of slip offshore. Furthermore, our model assumes that afterslip is driven by coseismic shear stress steps due to the main shock and the largest aftershock. However, numerical simulations employing a two-dimensional fault show that delayed stress build-up due to propagation of afterslip also affects evolution of afterslip [*Kato*, 2007; *Ariyoshi et al.*, 2007].

[50] We now turn to a discussion of the first question we posed in the Introduction, "Why was there a 1.2 hour delay in rapid acceleration of afterslip following the main shock?" We have demonstrated that the delay in rapid acceleration of afterslip can be reproduced by a model in which a patch of afterslip governed by rate-state friction nucleates in response to a sudden stress change. In this model, it is assumed that the afterslip region and the coseismic slip region do not overlap in space. This is inconsistent with numerical simulations with rate-state friction that show some overlap of dynamic rupture and afterslip. For example, the simulations carried out by *Lapusta and Rice* [2003] show rapid afterslip at the periphery of the coseismic slip region that is essentially prolonged deceleration of coseismic slip. In order for the spring-slider model of afterslip nucleation to be relevant, the coseismic rupture must be prevented somehow from propagating into the afterslip region, and the conditions for this to occur are not clear.

[51] Finally, we address the second question posed in the Introduction, "Did the main shock or the largest aftershock trigger the afterslip?" Figure 16b shows slip velocity histories computed from the same parameter values as those used in Figure 15 except for $\Delta\tau_{aft}$, which is assumed to be zero. In other words, Figure 16b shows slip velocity histories contributed only by the main shock for the four cases shown in Figure 15. In all the cases corresponding to $\Delta\tau_{aft} < 0.4$ MPa (red, blue, and black curves in Figure 16b), the rapid acceleration of afterslip due to the stress change only from the main shock occurs at about 1.2 hours after the main shock. Hence the timing of the rapid acceleration of

afterslip is independent of the timing of the largest aftershock. However, comparison of Figure 16 with Figure 15 clearly shows that the stress change due to the largest aftershock contributes substantially to the amount of afterslip. Figure 15 and Figure 16 also show that, for $\Delta\tau_{\mathrm{aft}} \geq 0.4$ MPa, the largest aftershock is large enough to control the timing of the rapid acceleration of afterslip, and therefore the largest aftershock could be considered the trigger of afterslip. However, this requires that $\Delta\tau_{\mathrm{aft}}$ is at least five times larger than inferred from our slip model. This suggests that the timing of the rapid acceleration of afterslip is probably controlled by the frictional properties of the fault and stress change from the main shock, not by the timing of the largest aftershock.

6. Conclusions

[52] We model early postseismic deformation following the 2003 Tokachi-oki earthquake captured by subdaily GPS data assuming that the observed GPS signal is a response to afterslip on the subduction interface. The data show little motion immediately after the main shock with sudden acceleration at about 1.2 hours following the main shock at the time of the largest aftershock. We show that a model assuming that early afterslip is a response of a fault patch to instantaneous stress perturbations caused by the main shock and the largest aftershock can reproduce the observed GPS time series data. Early afterslip on the fault patch is modeled with a single-degree-of-freedom spring-slider model obeying a rate- and state-dependent friction law. We develop an inversion method to estimate the posterior probability distributions of the friction parameters D_c, $a\sigma$, and $(a - b)\sigma$ and the spring stiffness k from the postseismic GPS time series. The estimated 95% confidence intervals of D_c, $a\sigma$, and $(a - b)\sigma$ are 2.6×10^{-4}–1.8×10^{-3} m, 0.29–0.43 MPa, and 0.214–0.220 MPa, respectively, if we adopt stress changes from the main shock and the largest aftershock inferred from kinematic slip inversions of coseismic GPS displacements and assume pre-earthquake slip rate that is half of the rate of the Pacific plate subduction. The estimated values of D_c are 10 to 10^3 times larger than typical laboratory values. The estimated values of $a\sigma$ and $(a - b)\sigma$ are 1 to 2 orders of magnitude smaller than values obtained from typical laboratory values of a and $a - b$ and effective normal stress given by lithostatic pressure minus hydrostatic pore pressure, indicating that a and $a - b$ are smaller than typical laboratory values and/or the pore pressure on the plate boundary is significantly elevated above the hydrostatic value.

[53] We find that uncertainties in stress change due to the main shock and pre-earthquake slip rate have marginal effects on estimates and uncertainties of $a\sigma$, $(a - b)\sigma$, and k but do not affect estimates and uncertainties of D_c if the main shock–induced stress change is between 1–3 MPa and pre-earthquake slip rate is smaller than the rate of plate subduction. Uncertainties in stress change due to the largest aftershock also affects estimates and uncertainties of D_c, $a\sigma$, $(a - b)\sigma$, and k. Although the time of the rapid acceleration of afterslip coincides with the time of the largest aftershock, our analyses suggest that the timing of the rapid acceleration of afterslip is controlled by the frictional properties of the fault and stress change from the main shock, not by the timing of the largest aftershock.

Appendix A: Monte Carlo Sampling of the Posterior PDF

[54] In this appendix, we illustrate the Metropolis algorithm that generates samples from the posterior PDF, $p(\mathbf{m}|\mathbf{d})$, given by equation (18). For a detailed explanation of the MCMC methods including the Metropolis algorithm, we refer the reader to other texts on the topic [e.g., *Gamerman*, 1997; *MacKay*, 2003]. The Metropolis algorithm samples the posterior PDF by exploring the model space using a Markov chain random walk which is designed to converge to the posterior PDF. More specifically, the Metropolis algorithm iterates the following procedure many times. Let $\mathbf{m}^{(i)}$ be the model at ith iteration. The Metropolis algorithm generates the next model, $\mathbf{m}^{(i+1)}$, by a two-step procedure. The first step generates a candidate model, $\mathbf{m}'$, by perturbing the current model, $\mathbf{m}^{(i)}$, by a Markov chain random walk in which the probability of visiting $\mathbf{m}'$ depends only on the current model $\mathbf{m}^{(i)}$ and not on previously visited models. In our implementation, the model $\mathbf{m}'$ is generated from $\mathbf{m}^{(i)}$ by randomly perturbing $\mathbf{m}^{(i)}$ along the jth coordinate axis in the model space

$$\mathbf{m}' = \mathbf{m}^{(i)} + r_i \Delta m_j \mathbf{e}_j, \tag{A1}$$

where r_i is a $[-1, 1]$ uniform random number, Δm_j is the step size of the random walk for the jth component of $\mathbf{m}$, and $\mathbf{e}_j$ is the unit vector along the jth axis in the model parameter space. The index j, that specifies the direction to which $\mathbf{m}^{(i)}$ is perturbed, is varied in sequential order. In the second step, the candidate $\mathbf{m}'$ is accepted as the next model (i.e., $\mathbf{m}^{(i+1)} = \mathbf{m}'$) with a probability determined by the posterior probability densities of the candidate and the current models

$$P_{\mathrm{accept}} = \min\left[1, \frac{p(\mathbf{m}'|\mathbf{d})}{p(\mathbf{m}^{(i)}|\mathbf{d})}\right]. \tag{A2}$$

If the candidate model is not accepted, the random walk remains at the current model: $\mathbf{m}^{(i+1)} = \mathbf{m}^{(i)}$. Note that it is necessary to solve the forward problem (equations (2), (5), and (13)) to evaluate $p(\mathbf{m}'|\mathbf{d})$. We do not need to evaluate $p(\mathbf{m}^{(i)}|\mathbf{d})$ in this iteration because it has already been calculated in the previous iteration. Therefore it is necessary to solve the forward problem once in a single iteration. It should also be noted that we do not need to calculate the normalizing constant c in equation (18) when we evaluate $p(\mathbf{m}'|\mathbf{d})$ because the acceptance probability P_{accept} depends on the ratio of the probability densities, not the probability density itself. Iterations of the two-step procedure from a starting model $\mathbf{m}^{(0)}$ produce a sequence of model parameter vectors, $\{\mathbf{m}^{(0)}, \mathbf{m}^{(1)}, \ldots\}$, that can be considered to be samples drawn from the posterior PDF, $p(\mathbf{m}|\mathbf{d})$.

[55] Early samples from the Metropolis algorithm may be influenced by a starting model, $\mathbf{m}^{(0)}$, and, in this case, they cannot be considered to be samples generated from the posterior PDF. This early period is regarded as a transient period during which the random walk gradually approaches

the high posterior probability region. It is necessary to discard these early samples to correctly obtain samples drawn from the posterior PDF. In addition, there is a correlation between $\mathbf{m}^{(i)}$ and $\mathbf{m}^{(i+1)}$ because $\mathbf{m}^{(i+1)}$ is generated from $\mathbf{m}^{(i)}$; hence, $\mathbf{m}^{(i)}$ and $\mathbf{m}^{(i+1)}$ are not independent samples from the posterior PDF. To obtain independent samples, it is necessary to collect samples with a sufficiently large interval. By collecting samples after sufficiently large number of iterations with large interval, the collected samples can be regarded as independent samples drawn from the posterior PDF, $p(\mathbf{m}|\mathbf{d})$.

[56] In our implementation of the Metropolis algorithm, we generate 5.65×10^6 samples and discard the first 5.0×10^4 samples to avoid the influence of a starting model. We then retain one of every 100 samples from the subsequent 5.6×10^6 samples to minimize the effect of correlation between successive samples and regard the 5.6×10^4 retained samples as independent samples from the posterior PDF.

[57] The step size of the Markov chain random walk, Δm_i, in equation (A1) controls the efficiency of the Metropolis algorithm. If Δm_i is too large, probability density of the candidate model, $p(\mathbf{m}'|\mathbf{d})$, is likely to be low and the acceptance probability, P_{accept}, is low. In this case the random walk is likely to remain at the current model for many iterations, and therefore the rate of convergence to the posterior PDF is slow. If Δm_i is too small, it takes a large number of iterations for the random walk to explore the entire high posterior probability regions of the model parameter space and therefore the rate of convergence to the posterior PDF is slow. Thus we implement the Metropolis algorithm many times employing various Δm_i until we identify Δm_i that samples the posterior PDF efficiently. As the step sizes for D_c, $a\sigma$, $(a - b)\sigma$, and k in the inversion shown in section 4.1, we use 5.0×10^{-2} m, 2.0×10^{-3} MPa, 2.0×10^{-4} MPa, and 5.0×10^{-2} MPa/m, respectively.

[58] **Acknowledgments.** We are grateful to Hugo Perfettini, an anonymous reviewer, and the Associate Editor for their helpful reviews and comments that helped to improve the manuscript. J.F. and K.J. were supported by NSF grant EAR-0635741. K.L. acknowledges support from EAR-0538116 and EAR-0609646. We thank the Geographical Survey Institute for providing the GPS data. Some of the figures were created using generic mapping tools [*Wessel and Smith*, 1998].

References

Akaike, H. (1980), Likelihood and the Bayes procedure, in *Bayesian Statistics*, edited by J. M. Bernardo, et al., pp. 143–166, University Press, Valencia, Spain.

Ariyoshi, K., T. Matsuzawa, and A. Hasegawa (2007), The key frictional parameters controlling spatial variations in the speed of postseismic-slip propagation on a subduction plate boundary, *Earth Planet. Sci. Lett.*, *256*, 136–146, doi:10.1016/j.epsl.2007.01.019.

Baba, T., K. Hirata, T. Hori, and H. Sakaguchi (2006), Offshore geodetic data conducive to the estimation of the afterslip distribution following the 2003 Tokachi-oki earthquake, *Earth Planet. Sci. Lett.*, *241*, 281–292, doi:10.1016/j.epsl.2005.10.019.

Blanpied, M. L., D. A. Lockner, and J. D. Byerlee (1995), Frictional slip of granite at hydrothermal conditions, *J. Geophys. Res.*, *100*(B7), 13,045–13,064.

Blanpied, M. L., C. J. Marone, D. A. Lockner, J. D. Byerlee, and D. P. King (1998), Quantitative measure of the variation in fault rheology due to fluid-rock interactions, *J. Geophys. Res.*, *103*(B5), 9691–9712.

DeMets, C., R. G. Gordon, D. F. Argus, and S. Stein (1994), Effect of recent revisions to the geomagnetic reversal timescale on estimates of current plate motions, *Geophys. Res. Lett.*, *21*(20), 2191–2194.

Dieterich, J. H. (1979), Modeling of rock friction: 1. Experimental results and constitutive equations, *J. Geophys. Res.*, *84*(B5), 2161–2168.

Dieterich, J. H. (1981), Constitutive properties of faults with simulated gouge, in *Mechanical Behavior of Crustal Rocks*, *Geophys. Monogr. Ser.*, vol. 24, edited by N. L. Carter et al., pp. 103–120, AGU, Washington, D. C.

Dieterich, J. H. (1986), A model for the nucleation of earthquake slip, in *Earthquake Source Mechanics*, *Geophys. Monogr. Ser.*, vol. 37, edited by S. Das, J. Boatwright, and C. H. Scholz, pp. 37–47, AGU, Washington, D. C.

Earthquake Research Committee (2003), *Long-term Evaluation of Earthquakes Along the Kurile Trench* (in Japanese), Headquarters for Earthquake Research Promotion, Tokyo, Japan. (Available at http://www.jishin.go.jp/main/chousa/03mar_chishima/index.htm)

Gamerman, D. (1997), *Markov Chain Monte Carlo: Stochastic Simulation for Bayesian Inference*, 245 pp., CRC Press, Boca Raton, Fla.

Gu, J.-C., J. R. Rice, A. L. Ruina, and S. T. Tse (1984), Slip motion and stability of a single degree of freedom elastic system with rate and state dependent friction, *J. Mech. Phys. Solids*, *32*, 167–196.

Hastings, W. K. (1970), Monte Carlo sampling methods using Markov chains and their applications, *Biometrika*, *57*, 97–109.

Hearn, E. H., R. Bürgmann, and R. E. Reilinger (2002), Dynamics of İzmit earthquake postseismic deformation and loading of the Düzce earthquake hypocenter, *Bull. Seismol. Soc. Am.*, *92*, 172–193, doi:10.1785/0120000832.

Hori, T., N. Kato, K. Hirahara, T. Baba, and Y. Kaneda (2004), A numerical simulation of earthquake cycles along the Nankai Trough in southwest Japan: Lateral variation in frictional property due to the slab geometry controls the nucleation position, *Earth Planet. Sci. Lett.*, *228*, 215–226, doi:10.1016/j.epsl.2004.09.033.

Hsu, Y.-J., M. Simons, J.-P. Avouac, J. Galetzka, K. Sieh, M. Chlieh, D. Natawidjaja, L. Prawirodirdjo, and Y. Bock (2006), Frictional afterslip following the 2005 Nias-Simeulue earthquake, Sumatra, *Science*, *312*, 1921–1926, doi:10.1126/science.1126960.

Johnson, K. M., R. Bürgmann, and K. M. Larson (2006), Frictional properties on the San Andreas fault near Parkfield, California, inferred from models of afterslip following the 2004 earthquake, *Bull. Seismol. Soc. Am.*, *96*, S321–S338, doi:10.1785/0120050808.

Johnson, K. M., R. Bürgmann, and J. T. Freymueller (2009), Coupled afterslip and viscoelastic flow following the 2002 Denali fault, Alaska earthquake, *Geophys. J. Int.*, *176*, 670–682, doi:10.1111/j.1365-246X.2008.04029.x.

Kato, N. (2004), Interaction of slip on asperities: Numerical simulation of seismic cycles on a two-dimensional planar fault with nonuniform frictional property, *J. Geophys. Res.*, *109*, B12306, doi:10.1029/2004JB003001.

Kato, N. (2007), Expansion of aftershock areas caused by propagating postseismic sliding, *Geophys. J. Int.*, *168*, 797–808, doi:10.1111/j.1365-246X.2006.03255.x.

Kato, N. (2008), Numerical simulation of recurrence of asperity rupture in the Sanriku region, northeastern Japan, *J. Geophys. Res.*, *113*, B06302, doi:10.1029/2007JB005515.

Kato, N., and T. Hirasawa (1999), A model for possible crustal deformation prior to a coming large interplate earthquake in the Tokai district, central Japan, *Bull. Seismol. Soc. Am.*, *89*, 1401–1417.

Katsumata, K., N. Wada, and M. Kasahara (2003), Newly imaged shape of the deep seismic zone within the subducting Pacific plate beneath the Hokkaido corner, Japan-Kurile arc-arc junction, *J. Geophys. Res.*, *108*(B12), 2565, doi:10.1029/2002JB002175.

Lapusta, N., and J. R. Rice (2003), Nucleation and early seismic propagation of small and large events in a crustal earthquake model, *J. Geophys. Res.*, *108*(B4), 2205, doi:10.1029/2001JB000793.

Larson, K. M., and S. Miyazaki (2008), Resolving static offsets from high-rate GPS data: The 2003 Tokachi-oki earthquake, *Earth Planets Space*, *60*, 801–808.

Linker, M., and J. Rice (1997), Models of postseismic deformation and stress transfer associated with the Loma Prieta earthquake, in *The Loma Prieta, California Earthquake of October 17, 1989: Aftershocks and Postseismic Effects*, *U.S. Geol. Surv. Prof. Pap.*, *1550-D*, edited by P. A. Reasenberg, pp. D253–D275, U.S. Gov. Print. Off., Washington, D. C.

Liu, Y., and J. R. Rice (2005), Aseismic slip transients emerge spontaneously in three-dimensional rate and state modeling of subduction earthquake sequences, *J. Geophys. Res.*, *110*, B08307, doi:10.1029/2004JB003424.

Liu, Y., and J. R. Rice (2007), Spontaneous and triggered aseismic deformation transients in a subduction fault model, *J. Geophys. Res.*, *112*, B09404, doi:10.1029/2007JB004930.

MacKay, D. J. C. (2003), *Information Theory, Inference, and Learning Algorithms*, 628 pp., Cambridge Univ. Press, New York.

Marone, C. (1998), Laboratory-derived friction laws and their application to seismic faulting, *Annu. Rev. Earth Planet. Sci.*, *26*, 643–696.

Marone, C., and B. Kilgore (1993), Scaling of the critical slip distance for seismic faulting with shear strain in fault zones, *Nature*, *362*, 618–621.

Marone, C. J., C. H. Scholtz, and R. Bilham (1991), On the mechanics of earthquake afterslip, *J. Geophys. Res.*, *96*(B5), 8441–8452.

Metropolis, N., A. W. Rosenbluth, M. N. Rosenbluth, A. H. Teller, and E. Teller (1953), Equation of state calculations by fast computing machines, *J. Chem. Phys.*, *21*, 1087–1092.

Miura, S., Y. Suwa, A. Hasegawa, and T. Nishimura (2004), The 2003 M8.0 Tokachi-Oki earthquake – How much has the great event paid back slip debts?, *Geophys. Res. Lett.*, *31*, L05613, doi:10.1029/2003GL019021.

Miyazaki, S., and K. M. Larson (2008), Coseismic and early postseismic slip for the 2003 Tokachi-oki earthquake sequence inferred from GPS data, *Geophys. Res. Lett.*, *35*, L04302, doi:10.1029/2007GL032309.

Miyazaki, S., P. Segall, J. Fukuda, and T. Kato (2004), Space time distribution of afterslip following the 2003 Tokachi-oki earthquake: Implications for variations in fault zone frictional properties, *Geophys. Res. Lett.*, *31*, L06623, doi:10.1029/2003GL019410.

Miyazaki, S., P. Segall, J. Fukuda, K. M. Johnson, and T. Kato (2006), Postseismic deformation following two thrust earthquakes at Kurile-Japan Trench: The 2003 Tokachi-oki and the 2005 Miyagi-oki earthquakes, *Eos Trans. AGU*, *87*(52), Fall Meet. Suppl., Abstract G31A-05.

Montési, L. G. J. (2004), Controls of shear zone rheology and tectonic loading on postseismic creep, *J. Geophys. Res.*, *109*, B10404, doi:10.1029/2003JB002925.

Okada, Y. (1985), Surface deformation due to shear and tensile faults in a half-space, *Bull. Seismol. Soc. Am.*, *75*, 1135–1154.

Okada, Y. (1992), Internal deformation due to shear and tensile faults in a half-space, *Bull. Seismol. Soc. Am.*, *82*, 1018–1040.

Ozawa, S., M. Kaidzu, M. Murakami, T. Imakiire, and Y. Hatanaka (2004), Coseismic and postseismic crustal deformation after the M_w 8 Tokachi-oki earthquakes in Japan, *Earth Planets Space*, *56*, 675–680.

Paterson, M. S., and T.-F. Wong (2005), *Experimental Rock Deformation – The Brittle Field*, 2nd ed., 347 pp., Springer-Verlag, New York.

Perfettini, H., and J.-P. Ampuero (2008), Dynamics of a velocity strengthening fault region: Implications for slow earthquakes and postseismic slip, *J. Geophys. Res.*, *113*, B09411, doi:10.1029/2007JB005398.

Perfettini, H., and J.-P. Avouac (2004), Postseismic relaxation driven by brittle creep: A possible mechanism to reconcile geodetic measurements and the decay rate of aftershocks, application to the Chi-Chi earthquake, Taiwan, *J. Geophys. Res.*, *109*, B02304, doi:10.1029/2003JB002488.

Perfettini, H., and J.-P. Avouac (2007), Modeling afterslip and aftershocks following the 1992 Landers earthquake, *J. Geophys. Res.*, *112*, B07409, doi:10.1029/2006JB004399.

Perfettini, H., J.-P. Avouac, and J.-C. Ruegg (2005), Geodetic displacements and aftershocks following the 2001 M_w = 8.4 Peru earthquake: Implications for the mechanics of the earthquake cycle along subduction zones, *J. Geophys. Res.*, *110*, B09404, doi:10.1029/2004JB003522.

Ranjith, K., and J. R. Rice (1999), Stability of quasi-static slip in a single degree of freedom elastic system with rate and state dependent friction, *J. Mech. Phys. Solids*, *47*, 1207–1218.

Rice, J. R. (1993), Spatio-temporal complexity of slip on a fault, *J. Geophys. Res.*, *98*(B6), 9885–9907.

Rice, J. R., and J.-C. Gu (1983), Earthquake aftereffects and triggered seismic phenomena, *Pure Appl. Geophys.*, *121*, 187–219.

Ruina, A. (1983), Slip instability and state variable friction laws, *J. Geophys. Res.*, *88*(B12), 10,359–10,370.

Scholz, C. H. (1988), The critical slip distance for seismic faulting, *Nature*, *336*, 761–763.

Stuart, W. D. (1988), Forecast model for great earthquakes at the Nankai Trough subduction zone, *Pure Appl. Geophys.*, *126*, 619–641.

Stuart, W. D., and T. E. Tullis (1995), Fault model for preseismic deformation at Parkfield, California, *J. Geophys. Res.*, *100*(B12), 24,079–24,099.

Suwa, Y., S. Miura, A. Hasegawa, T. Sato, and K. Tachibana (2006), Interplate coupling beneath NE Japan inferred from three-dimensional displacement field, *J. Geophys. Res.*, *111*, B04402, doi:10.1029/2004JB003203.

Tse, S. T., and J. R. Rice (1986), Crustal earthquake instability in relation to the depth variation of frictional slip properties, *J. Geophys. Res.*, *91*(B9), 9452–9472.

Wessel, P., and W. H. F. Smith (1998), New, improved version of Generic Mapping Tools released, *Eos Trans. AGU*, *79*(47), 579.

Yabuki, T., and M. Matsu'ura (1992), Geodetic data inversion using a Bayesian information criterion for spatial distribution of fault slip, *Geophys. J. Int.*, *109*, 363–375.

Yamanaka, Y., and M. Kikuchi (2003), Source process of the recurrent Tokachi-oki earthquake on September 26, 2003, inferred from teleseismic body waves, *Earth Planets Space*, *55*, e21–e24.

J. Fukuda and K. M. Johnson, Department of Geological Sciences, Indiana University, 1001 East 10th Street, Bloomington, IN 47405, USA. (jfukuda@indiana.edu; kajjohns@indiana.edu)

K. M. Larson, Department of Aerospace Engineering Sciences, University of Colorado, UCB 429, Boulder, CO 80309, USA. (kristinem.larson@gmail.com)

S. Miyazaki, Department of Geophysics, Graduate School of Science, Kyoto University, Kitashirakawa Oiwake-cho, Sakyo-ku, Kyoto 606-8502, Japan. (shinichi.miyazaki@kugi.kyoto-u.ac.jp)